PHYSICOCHEMICAL AND ELECTROCATALYTIC STUDIES OF SnO_2-GUAR GUM NANOCOMPOSITE

A Major Project Submitted In the Partial Fulfillment of the Requirement

For the Award of the degree of

MASTER OF TECHNOLOGY

IN

POLYMER TECHNOLOGY

Under the Supervision of

Prof. D.KUMAR

(Project Guide & Head)

Department of Applied Chemistry

& Polymer Technology

Delhi Technological University

Delhi - 110042

BY

PRIYA MALIK

(2K12/PTE/11)

DEPARTMENT OF APPLIED CHEMISTRY & POLYMER TECHNOLOGY

DELHI TECHNOLOGICAL UNIVERSITY, DELHI- 110042

DELHI TECHNOLOGICAL UNIVERSITY

(Govt. of National Capital Territory of Delhi)

Shahbad Daulatpur, Main Bawana Road,

Delhi - 110042

CERTIFICATE

This is to certify that Ms. Priya Malik has Satisfactorily Completed this Major project entitled "Physicochemical and Electrocatalytic Studies of SnO_2-Guar Gum Nanocomposite" in the Partial Fulfillment for the Award of the Degree of Master of Technology in Polymer Technology of Delhi Technological University, Delhi During the Academic Session 2014.

To the Best of my knowledge and Belief, this Work has not been submitted to any other University or Institutions for the Award of any Degree or Diploma.

Prof. D. Kumar

Project Guide & Head

Department of Applied Chemistry &

Polymer Technology,

DTU, Delhi-110042

ACKNOWLEDGEMENT

Taking the opportunity of this column, I would like to express my sincere gratitude to all those who directly or indirectly helped me in successful completion of my project.

First of all I heartedly express my humble gratitude to **Prof. D.KUMAR**, Department of Applied Chemistry & Polymer Technology, Delhi Technological University (Formerly Delhi College of Engineering), for providing me the facilities, guidance, suggestions and constant encouragement throughout the tenure of my project work. I am deeply indebted to him for giving me an opportunity to work with him and helping me in every possible way in bringing out this work to reality.

I also would like to express any sincere gratitude to **Dr. Jay Singh**, Department of Applied Chemistry & Polymer Technology, Delhi Technological University (Formerly Delhi College of Engineering), complete my entire project under their valuable guidance, constant support and encouragements.

I am also thankful to Dr. Sameer Sapra, Professor Department of Chemistry, Indian Institute of Technology, Delhi, for his kind assistance for providing XRD spectra.

I like to express my sincere thanks to Department of Anatomy, All India Institute of Medical Sciences, New Delhi, for providing TEM analysis for my Metal oxide samples.

I am very much thankful to Dr. Pamela Singh, Department of Biotechnology, Murthal, for carrying out antibacterial study.

I am thankful to Mr. Ratnesh and Mr. Vinay, Research Scholar Department of Applied Physics, Delhi Technology University, New Delhi, for providing AFM spectra and PL spectra.

I also express my deep sense of gratitude to Ms. Reetu Prabhakar, Ms. Sarita S. Nair and Ms. Nidhi, Research Scholar Department of Applied Chemistry and Polymer Technology for their kind discussion and valuable suggestion.

I am grateful to all the staff members of the Department of Applied Chemistry and Polymer Technology (Formerly Delhi College of Engineering), Delhi Technological University for their kind help in various occasions in my Project work.

I would like to extend our thanks to all the non-teaching staff of the Polymer Technology Department, especially Mr. Aman and Mr. Sandeep of Polymer Department.

I am thankful to all my colleagues (friends) Manish Kumar and Alkesh Kumari whose inspiring suggestion and ceaseless enthusiasm for the topic explored in this thesis has meant a great deal to me.

Last, but not the least, my parents, my brother and my well-wishers have been with me at every step of this exciting journey. I thank them for all their prayers, encouragements and best wishes.

Date:

PRIYA MALIK
2K12/PTE/11
M.TECH (Polymer Technology)
Dept. of Applied Chemistry & Polymer Technology
DTU, Delhi-110042

UNDERTAKING

I declare that the work presented in this thesis titled "**Physicochemical and electrocatalytic studies of SnO_2-Guar gum nanocomposite**", submitted to the Department of Applied Chemistry & Polymer Technology, Delhi Technological University, for the award of the Master in Technology degree in Polymer Technology, is my original work. I have not plagiarized or submitted the same work for the award of any other degree either in this University or in any other University/Deemed University without proper citation. In case this undertaking is found incorrect, I accept that my degree may be unconditionally withdrawn.

Date:
Place: DTU, Delhi

Signature of the candidate

TABLE OF CONTENTS

LIST OF FIGURES

LIST OF TABLE

ABSTRACT

In this project report, I tried to present results of the studies related to fabrication of a metal oxide based efficient non-enzymatic sensor using an interface based on sol-gel derived nanostructured tin oxide (SnO_2). A colloidal solution of prepared nanostructures has been electrophoretically deposited (EPD) onto an indium-tin-oxide (ITO) glass substrate. The structural and morphological studies of SnO_2 nanoparticles have been carried out by X-ray diffraction (XRD) (particle size 10.6 nm) , scanning electron microscopy (SEM), transmission electron microscopy (TEM), atomic force microscopy (AFM), UV-visible spectroscopy (UV-Vis), photoluminescence spectroscopy (PL) and Fourier transform infrared (FTIR) spectroscopic techniques. Guar gum (a biopolymer) was used as a matrix to prepare the nanocomposite. The SnO_2 nanoparticles were then ultrasonically dispersed in guar gum (GG) solution, and then used to form SnO_2-GG nanocomposite film by drop casting method on the ITO plate. The SnO_2-GG/ITO nanocomposite film was found to provide improved sensing characteristics to the electrode interface in terms of electroactive surface area, diffusion coefficient, charge transfer rate constant and electron transfer kinetics. This interfacial platform has been used for fabrication of a non-enzymatic sensor for hydrazine sensing. The results of response studies of the fabricated SnO_2-GG/ITO electrode show a linear range of 2-22 mM, detection limit of 2.769 mM, and high sensitivity of 5.72 μMcm^{-2} with a response time of 35 s. The utilization of this SnO_2 modified electrode for electo-oxidation of hydrazine offers an efficient strategy and a novel interface for application of tin oxide in the field of electrochemical sensors.

1. Introduction

Nanotechnology is one of the leading scientific fields today since it combines knowledge from the fields of Physics, Chemistry, Biology, Medicine, Informatics, and Engineering. It is an emerging technological field with great potential to lead in great breakthroughs that can be applied in real life. Novel nano and biomaterials, and nanodevices are fabricated and controlled by nanotechnology tools and techniques, which investigate and tune the properties, responses, and functions of living and non-living matter, at sizes below 100 nm [1]. The term nanotechnology comes from the combination of two words: the Greek numerical prefix nano referring to a billionth and the word technology. As an outcome, nanotechnology or nanoscaled technology is generally considered to be at a size below 0.1 μ or 100 nm (a nanometer is one billionth of a meter, 10^{-9} m). Nanoscale science (or nanoscience) studies the phenomena, properties, and responses of materials at atomic, molecular, and macromolecular scales, and in general at sizes between 1 and 100 nm. In this scale, and especially below 5 nm, the properties of matter differ significantly (i.e., quantum-scale effects play an important role) from that at a larger particulate scale. Nanotechnology is then the design, the manipulation, the building, the production and application, by controlling the shape and size, the properties-responses and functionality of structures, and devices and systems of the order or less than 100 nm [2, 3].

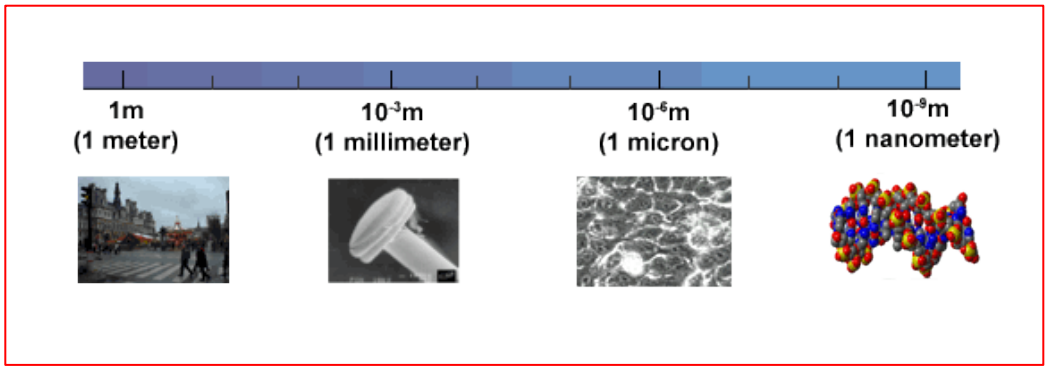

Figure 1.1: Schematic diagram showing nano on scale

Different methods for the synthesis of nano-engineered materials and devices can accommodate precursors from solid, liquid or gas phases and encompass a tremendously varied set of experimental techniques. In general, however, most synthetic methods can be classified into two

main approaches: "*top-down*" and "*bottom-up*" approaches and combinations of them (Fig. 1.2). "*Top-down*" (photolithography, microcontact printing) techniques begin with a macroscopic material or group of materials and incorporate smaller-scale details into them, whereas "*bottom-up*" (organic-synthesis, self-assembly) approaches begin by designing and synthesizing custom-made molecules that have the ability to self-assemble or self-organize into higher order mesoscale and macroscale structures. Bottom-up approach aims to guide the assembly of atomic and molecular constituents into organized surface structures through processes inherent in the manipulated system [4]. Fig 1.2 shows (clockwise from top) approaches to control matter at the nanoscale are top down approach and bottom up approach an electron microscopy image of a nanomechanical electrometer obtained by electron-beam lithography, patterned films of carbon nanotubes obtained by microcontact printing and catalytic growth, a single carbon nanotube connecting two electrodes, a regular metal-organic nanoporous network integrating iron atoms and functional molecules, and seven carbon monoxide molecules forming the letter "C" positioned with the tip of a scanning tunneling microscope [4].

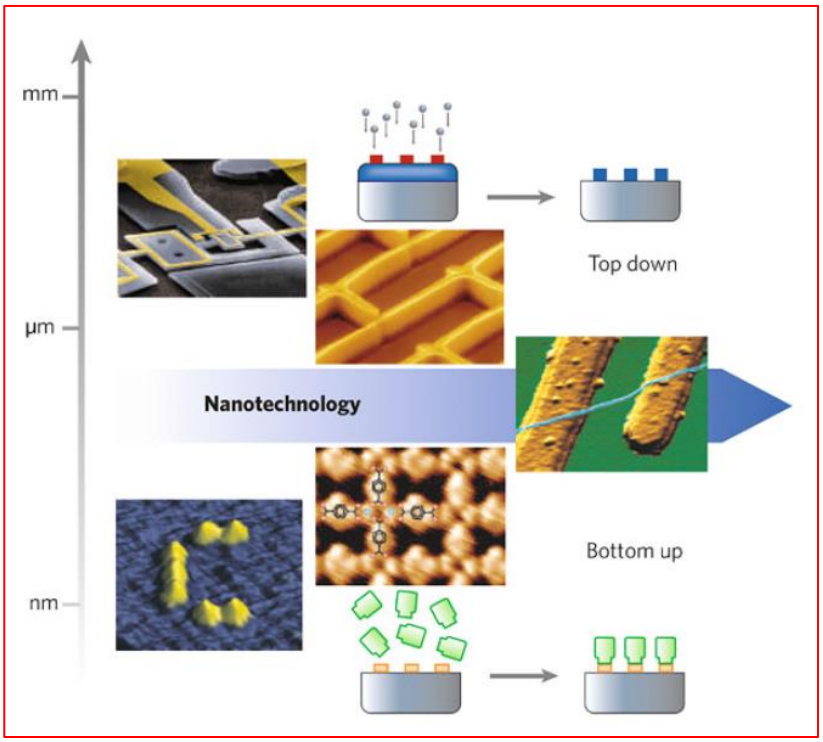

Figure 1.2: Schematic diagram to show to different approaches to control matter at the nanoscale level: top down and bottom up approach

1.1 Tin oxide (SnO_2) - physical structure

Tin dioxide, also as tin (IV) oxide and stannic oxide, is the inorganic compound with the formula SnO_2. The mineral form of SnO_2 is called cassiterite, and this is the main ore of tin. This colorless, diamagnetic solid is amphoteric. It crystallizes with the rutile structure, wherein the tin atoms are six coordinate and the oxygen atoms three coordinate. SnO_2 is usually regarded as an oxygen-deficient n-type semiconductor.

Rutile has a body-centered tetragonal unit cell, with unit cell parameters a = b = 4.584 Å, and c = 2.953 Å. The titanium cations have a coordination number of 6 meaning they are surrounded by an octahedron of 6 oxygen atoms. The oxygen anions have a co-ordination number of 3 resulting in a trigonal planar co-ordination. Rutile also shows a screw axis when its octahedra are viewed sequentially.

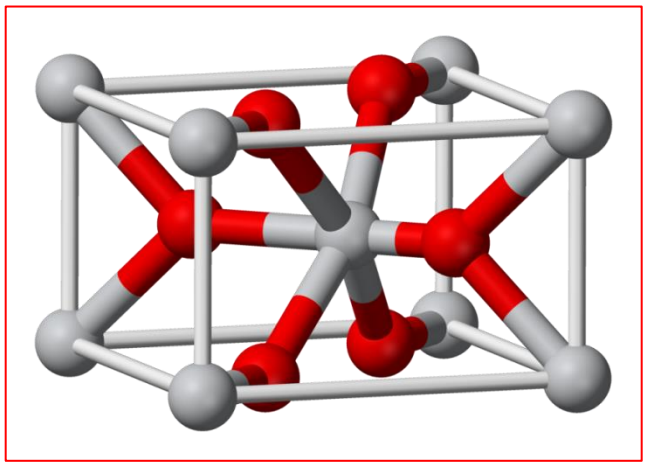

Figure 1.3: The unit cell of rutile (SnO_2)

1.2 SnO_2 nanoparticle synthesis

Tin dioxide (SnO_2) is an important oxide semiconductor material, which has been widely used in many applications such as catalysts agent [5,6], hazardous gas sensors [7,8], heat reflecting mirrors [9,10], varistors [11,12], transparent conducting electrodes for solar cells

[13,14], and optoelectronic devices [15]. Tin dioxide-based gas sensor devices are very important in developing n-type semiconductor sensors, which can be utilized to detect various inflammable and harmful gases such as hydrogen (H_2), carbon monoxide (CO), ethanol and methanol. Semiconductor sensors exhibit changes in electrical resistivity in the presence of small concentrations of certain gases. Sensors consisting of fine particles of metal oxides usually exhibit high sensitivity compared to their counterparts made of larger particles. The most important factor affecting the sensitivity of gas sensors is the actual crystallite size of the sensing materials.

Dong-Feng Zhang et al have done the low temperature fabrication of highly crystalline SnO_2 nanorods. SnO_2 is a stable and large band gap semiconductor very well known for its excellent gas sensitivity. It has also been widely used for the transistors, electrode materials and solar cells [16-18]. SnO_2 nanocrystals have been synthesized by a number of methods including sol-gel, hydrothermal, chemical deposition, magnetron sputtering and micro wave irradiation processes. However, most of the methods have produced films and nanocrystals. This group has successfully fabricated uniform SnO_2 nanorods by a one-step procedure under mild conditions. They also performed the XRD, SEM, TEM, HRTEM and EDX to characterize the SnO_2 nanorods.

Madzlan Aziz et al have performed the size controlled synthesis of SnO_2 nanoparticles by sol-gel method. Tetragonal phase of SnO_2 nanoparticles were synthesized by sol-gel method using stannous chloride ($SnCl_2.2H_2O$) and polyethylene glycol (PEG) at different calcination temperatures. The phase, size and purity of the resultant SnO_2 nanoparticles were characterized by XRD. The morphological details were confirmed with the FESEM analysis [19].

A. Ayeshamariam et al have synthesized SnO_2 nanoparticles and did their structural and optical characterizations. They have produced nanocrystalline oxide powders through a simple and inexpensive route. The sol-gel combustion process was followed to prepare SnO_2 powder. The prepared powders were characterized for their structural, morphological, electrical and gas sensor properties for ethanol. Crystal density, lattice volume and microstrain were found to be nearly constant with annealing temperature, which confirm the formation of monophase SnO_2.

Spherical particles in the nanoscale level, with the size increasing with temperature are observed from XRD, SEM and TEM results [20].

Ganesh E Patil et al have prepared the SnO_2 nanoparticles through hydrothermal route and performed their characterizations. The synthesis of SnO_2 nanoparticles was done using a simple hydrothermal route in the presence of the surfactant hydrazine at 100 °C for 12 h. X-ray diffraction (XRD), field emission scanning electron microscopy, and transmission electron microscopy (TEM) were employed to characterize the as-prepared product, and optical property was studied by UV-visible diffuse reflectance spectroscopy (DRS). The XRD pattern of the prepared sample was indexed to the tetragonal structure of SnO_2, and the calculated particle size was found to be 22.4 nm, which was further confirmed by TEM [21].

1.3 Guar gum – chemical structure and properties

Guar gum, also called guaran, is a galactomannan. It is primarily the ground endosperm of guar beans. The guar seeds are dehusked, milled and screened to obtain the guar gum. It is typically produced as a free-flowing, off-white powder. Guar gum is made up of non-ionic polydisperse rod-shaped polymers consisting of molecules (longer than found in locust bean gum) made up of about 10,000 residues. Higher galactose substitution also increases the stiffness (that is, decreases the flexibility) but reduces the overall extensibility and radius of gyration of the isolated chains [22]. The galactose residues prevent strong chain interactions as few unsubstituted clear areas have the minimum number (about 6) required for the formation of junction zones. Of the different possible galactose substitution patterns, the extremes of block substitution and alternating substitution give rise to the stiffer, with greater radius of gyration, and most flexible conformations respectively (random substitution being intermediate) [22]. Its persistence length is greater than that for locust bean gum at about 10 nm [23]. If the galactose residues were perfectly randomized, it unlikely that molecules would have more than one such area capable of acting as a junction zone, so disallowing gel formation. A block substitution pattern, for which there is some experimental evidence [24], would allow junction zone formation if the blocks were of sufficient length. Use of endo-1,4-β-D-mannanase and α-D-galactosidase have shown that shorter chain lengths and lower degrees of substitution lead to the formation of large, but soluble, assemblies while longer galactomannans have reduced solubility

[25]. Enzymatic hydrolysis of some of the galactose side chains may allow guar gum to be used to replace a dwindling locust bean gum supply. [26]

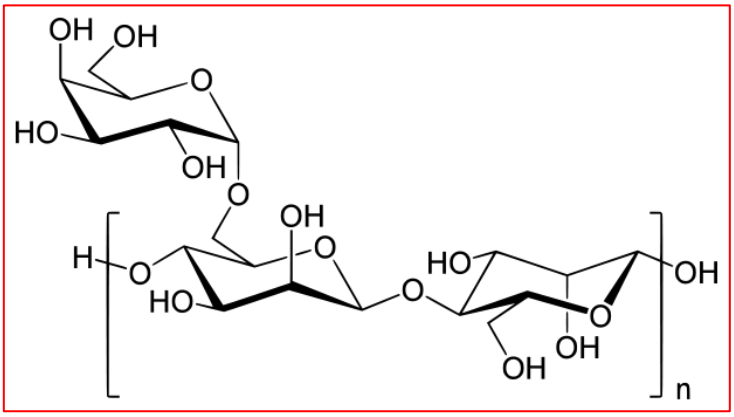

Figure 1.4: Chemical structure of GG

1.3.1 Advantages of GG

Guar gum is an economical thickener and stabilizer. It hydrates fairly rapidly in cold water to give highly viscous pseudoplastic solutions of generally greater low-shear viscosity when compared with other hydrocolloids and much greater than that of locust bean gum. High concentrations (~ 1%) are very thixotropic but lower concentrations (~ 0.3%) are far less so. Guar gum is more soluble than locust bean gum and a better emulsifier as it has more galactose branch points. Unlike locust bean gum, it does not form gels but does show good stability to freeze-thaw cycles. Guar gum shows high low-shear viscosity but is strongly shear-thinning. Being non-ionic, it is not affected by ionic strength or pH but will degrade at pH extremes at temperature (for example, pH 3 at 50 °C). It shows viscosity synergy with xanthan gum. With casein, it becomes slightly thixotropic forming a biphasic system containing casein micelles. Guar gum retards ice crystal growth non-specifically by slowing mass transfer across solid/liquid interface [27]. Unfortunately for the food industry, guar gum has been found to be ideal for use by the oil and gas industry to extract gas and oil from source rocks using pressurized fluid (hydraulic fracturing, or 'fracking'). This has increased both the demand for guar and its price several-fold [28].

1.4 SnO_2-polymer nanocomposite

Zhang Jing Chang et al. have described the synthesis of SnO_2/TiO_2 nanocomposite photocatalysts by supercritical fluid combination technology. This group has prepared the SnO_2/TiO_2 nanocomposite from $TiCl_4$ and $SnCl_4 \cdot 5H_2O$ by supercritical fluid combination technique (SCFCT). SCFCT is a combination of supercritical fluid drying method and sol-gel method. They have carried out different characterizations like XRD, FTIR and TEM. They showed that how a new kind of active particle (Ti, Sn) O_2 has formed and there is no sign of SnO_2 crystals observed in the range of the doping concentration studied. They evaluated the samples' photocatalytic activity by the degradation of acrylic acid. The results indicated that the SnO_2/TiO_2 nanocomposite photocatalysts prepared through SCFCT show significant improvement in catalytic activity as compared to pure TiO_2 or SnO_2/TiO_2 catalysts prepared by traditional drying (TD) [29].

A I. Aparnev et al have discussed the synthesis of nanocomposite materials in the SnO_2-NiO system. The group has synthesized the SnO_2-NiO nanocomposites with the specific surface area on the order of 100 m^2/g and the particle size of both phases of less than 10 nm by the sol-gel method with the subsequent annealing in the temperature interval 200–1000 °C. They showed that, with an increase in the annealing temperature to 900 °C, the specific surface area of the nanocomposites has increased. They had explained this effect by the increase in the porosity due to the destruction of the aggregates of primary amorphous particles [30].

V. S. Reddy Channu et al have fabricated a polyaniline-modified SnO_2 nanocomposite using solution route technique. The obtained pristine products were characterized with X-ray diffraction, thermogravimetric analysis, scanning electron microscopy, and optical absorption spectroscopy. Thermogravimetric analysis results showed that the polyaniline-modified SnO_2 nanoparticles exhibit higher thermal stability than the SnO_2 nanoparticles. Scanning electron microscopy analysis on the as-synthesized powders showed spherical particle in the range of 50 –100 nm [31].

1.5 GG based nanocomposite

Runa Ghosh Auddy et al have worked on the new guar biopolymer silver nanocomposites for wound healing. This group has worked on guar gum, a polymeric galactomannan that was intrinsically modified to a new cationic biopolymer guar gum alkylamine (GGAA) for wound healing applications. Biologically synthesized silver nanoparticles (Agnp) were further impregnated in GGAA for extended evaluations in punch wound models in rodents. SEM studies showed silver nanoparticles well dispersed in the new guar matrix [32].

Xiaoning Shi et al have worked on the Synthesis and enhanced swelling properties of a guar gum-based superabsorbent composite by the simultaneous introduction of styrene and attapulgite. They have prepared a series of novel guar gum-*graft*-poly(sodium acrylate-*co*-styrene)/attapulgite (GG-*g*-P(NaA-*co*-St)/APT) superabsorbent nanocomposites by the simultaneous graft copolymerization of partially neutralized acrylic acid (NaA), styrene (St) and attapulgite (APT) onto natural guar gum (GG), using ammonium per sulfate (APS) as the initiator and *N*,*N'*-methylene-*bis*-acrylamide (MBA) as the crosslinking agent. FTIR, UV and FESEM have been done to characterize the prepared nanocomposites [33].

1.6 SnO_2-GG nanocomposite

In this project, SnO_2-GG/ITO electrode was synthesized through the appropriate addition of SnO_2 nanostructures and GG solution by drop casting onto ITO electrode. The prepared electrode has been characterized by XRD, SEM, FTIR, UV-Vis, PL and electrochemical techniques for enhancing the electrocatalytic properties of hydrazine. This work provides an easy going and effective route for the synthesis of SnO_2-GG nanocomposite.

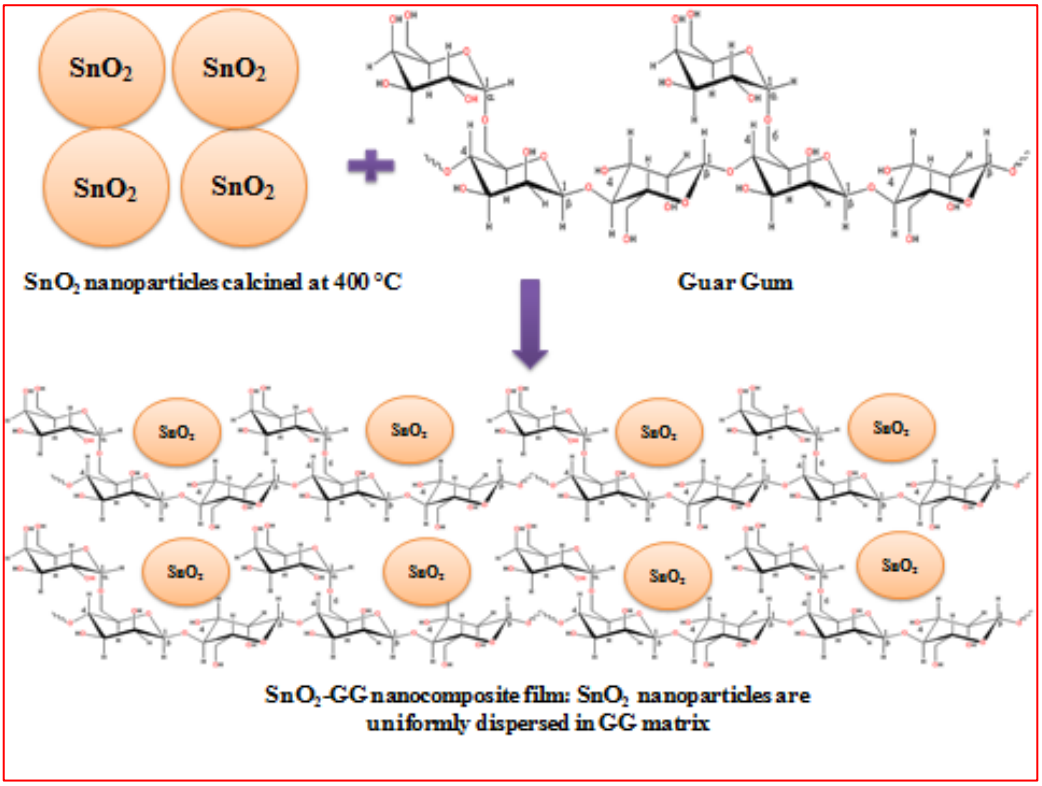

Figure 1.5: Schematic representation of SnO_2-GG nanocomposite preparation

1.7 Objective and methodology

For the fabrication of SnO_2-GG nanocomposite electrode for electro-oxidation study of hydrazine following experiments have been conducted:

(i) Synthesis of the Tin oxide (SnO_2) nanoparticles by sol-gel method

(ii) Particle size distribution and crystal size calculation of these nanoparticles through TEM and XRD

(iii) Preparation of thin film electrodes using various deposition techniques like electrochemical deposition, electrophoretic deposition (EPD)

(iv) Preparation of polymer solution and polymer based metal oxide nanocomposite film

(v) Fabrication of SnO_2-GG nanocomposite film electrode for sensing of hydrazine

(vi) Surface morphological studies and element analysis of the metal oxide based film electrodes and bioelectrodes using SEM, EDX and AFM

(vii) Bonding characteristics of these fabricated electrodes through FTIR studies

(viii) Amperometric measurements and electrochemical characterization like CV, DPV of these fabricated electrodes using potentiostat/galvanostat instrument

(ix) Electrochemical response studies of the bioelectrodes using sensing parameter like linearity, sensitivity, low detection limit, linear regression, and standard deviation

(x) Other electrochemical studies like effect of potential, pH, response time

1.7.1 Methodology adopted to achieve the above objective

To achieve the above objectives, we plan to follow the methodology described below**:**

(i) Synthesis of the SnO_2 nanoparticles using sol-gel method

(ii) Structure and crystal size calculation of SnO_2 nanoparticles through XRD

(iii) Preparation of polymer (guar gum) solution and guar gum based SnO_2 nanocomposite film on ITO

(iv) Drop casting for SnO_2-GG nanocomposite electrodes fabrication

(v) Surface morphological studies and element analysis of the electrodes using AFM, SEM, EDX

(vi) Bonding characteristics of those fabricated electrodes through FTIR

(vii) Amperometric measurement and electrochemical characterization like CV, and DPV

(viii) Electrochemical response studies of the nanocomposite electrodes using sensing parameter like linearity, sensitivity, low detection limit, linear regression, and standard deviation

(ix) Investigation of the effect of potential, pH, response time, stability on the fabricated nanocomposite electrode

(x) Application of prepared nanocomposite electrode for hydrazine sensing.

2. Materials and Methods

This chapter describes the various materials and methods used for the synthesis of SnO_2 nanoparticles and then the preparation of SnO_2-GG nanocomposite.

2.1 Materials

Stannous chloride ($SnCl_2.2H_2O$) and Sodium hydroxide pellets (NaOH) were obtained from Qualigens. Hydrochloric acid (HCl), Sodium phosphate monobasic (NaH_2PO_4), Sodium phosphate dibasic (Na_2HPO_4), Potassium ferrocyanide $\{K_4[Fe(CN)_6]\}$, Potassium ferricyanide $\{K_3[Fe(CN)_6]\}$, Sodium chloride (NaCl), Acetone (CH_3COCH_3) and Cetyl trimethyl ammonium bromide ($C_{19}H_{42}BrN$) were obtained from CDH (Delhi). Ammonia solution (NH_3) (25%), Hydrogen peroxide (H_2O_2) (30%) and Ethanol (C_2H_6O) were a product of Thomas Baker. Guar gum powder was obtained from Dabur India Ltd (viscosity 5000 cps). Nutrient agar was a product of HiMedia. The bacterial cultures of *B. cereus* and *P. aeruginosa* were procured from Department of Biotechnology, DCRUST, Murthal. The pre-cleaned hydrolyzed indium-tin-oxide (ITO) coated glass (Balzers) sheets of resistance 15 W/cm was used as the substrate for the deposition of composite electrode and treated as working electrodes. All other chemicals were of analytical grade and were used without further purification. The stock solutions of hydrazine (2-22 mM) were freshly prepared in phosphate buffer (5 mM, pH 7.0). Double distilled water has been deionized using Milli-Q water purification system (Milli-Q, USA).

2.2 Apparatus

X-ray diffraction (XRD) studies have been carried out to characterize the structure and particle size of SnO_2 nanoparticles and SnO_2-GG nanocomposite using Bruker D8 Advance Diffractometer with Ni-filtered Cu Kα radiation (IIT, New Delhi) with Voltage- 30 kV, 35 mA. The surface morphological studies of SnO_2, GG and SnO_2-GG film have been investigated using scanning electron microscope (HITACHI, Model No.S-3700N with EDS-X with X-ray). The atomic force microscopic studies have been done using Park Systems, XE-100. Transmission electron microscopy was done for the SnO_2 nanoparticles using FEI Tecnai S Twin (AIIMS,

New Delhi). Fourier transform infrared (FTIR) spectrophotometer (Thermoscientific, Nicolet-380) has been used to characterize SnO_2-GG nanocomposite. The UV-visible spectroscopic studies have been conducted on UV/VIS/NIR spectrometer (PerkinElmer, Lambda 950). The PL emission studies have been done using Fluorolog 3, made by Horiba. The electrochemical studies and amperometric measurements have been recorded on an Autolab Potentiostat/Galvanostat (Metrohm). The electrochemical measurements have been conducted on a three-electrode system with SnO_2-GG/ITO electrode as the working electrode, a platinum (Pt) wire as the counter electrode, and saturated Ag/AgCl electrode as a reference electrode in phosphate buffer saline (5 mM, pH 7.0, 0.9% NaCl) containing 5 mM $[Fe(CN)_6]^{3-/4-}$ mediator.

2.3 Methods

2.3.1 Synthesis of SnO_2 nanoparticles

The nanocrystalline SnO_2 nanoparticles have been prepared via sol-gel method. 0.2 M $SnCl_2.2H_2O$ was prepared in de-ionized water to form a uniform solution by stirring. An aqueous solution of ammonia (25%) was added drop wise into the obtained solution with steady stirring for 2 h, until pH of the final solution was reached to 12-13, and then a white precipitate was formed. 2 ml of 0.3 M C-TAB solution (surfactant) was added to above solution and the stirring was continued for 4-5 h. The uniform solution was then placed in a hot water bath at 50-60 °C for 2-3 h till the foam gets separated and the solution becomes transparent. Afterwards, the solution was quenched by dipping the solution beaker in cold water. Resulting mixture was filtered and washed several times with distilled water and ethanol till neutral pH is obtained. The resulting filtrate was then allowed to evaporate in the oven at 70-80 °C. The obtained white precipitate was calcined in Muffle furnace at 400 °C for 6 h. The obtained dried sample was then crushed and the obtained SnO_2 nanoparticles were filled in glass vial.

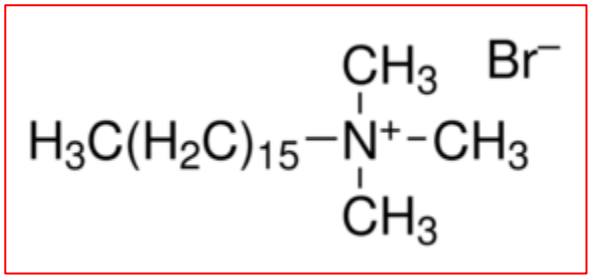

Figure 2.1: Chemical structure of cetyltrimethyl ammonium bromide

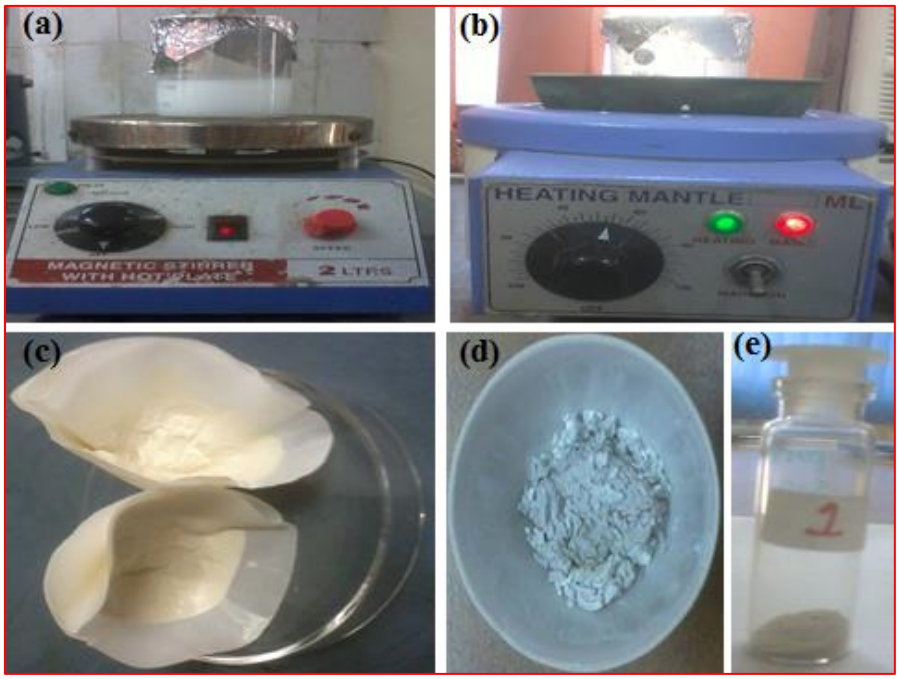

Figure 2.2: Steps followed for the synthesis of SnO_2 nanoparticles by sol-gel method: (a) mixing of $SnCl_2.2H_2O$ in DI water, (b) keeping in hot water bath after adding CTAB, (c) filtrate obtained after quenching, (d) SnO_2 nanoparticles after calcination and, (e) crushed SnO_2 nanoparticles for further testing

2.3.2 Functionalization of ITO (Indium Tin Oxide) glass substrate

ITO (Indium Tin Oxide) coated glass sheets were cut into small pieces (0.5 cm×2 cm) and immersed in a solution of H_2O_2:NH_3:H_2O in the ratio of 1:1:5 (v/v) respectively and then

kept under oven for 1 h at 80 °C to obtain uniformly distributed -OH groups on the ITO surface. Further the functionalized ITO plates were washed with de-ionized water and dried at room temperature. After that functionalized ITO plates were cleaned with acetone and stored in dust free environment and used in further steps of the project.

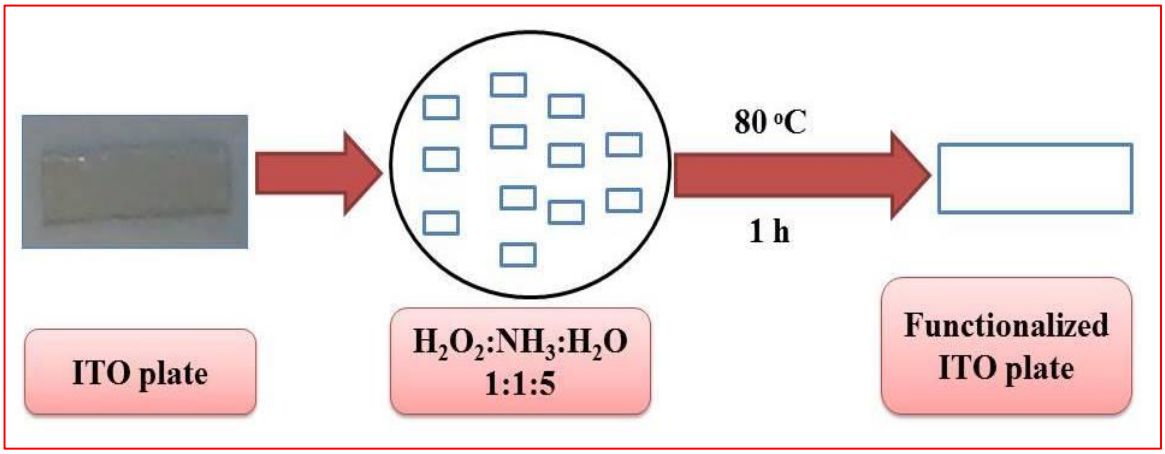

Figure 2.3: Schematic representation of functionalization of ITO plate

2.3.3 Electrophoretic deposition of SnO_2 nanoparticles on ITO electrode

Electrophoretic deposition (EPD) was carried out by using DC battery (Bio-Rad, model 200/2.0). The 25 mg SnO_2 nanostructure was dispersed in 5 ml of double DI water followed by ultrasonication (30 min). A platinum foil (1 cm×2 cm) was used as the cathode and a hydrolyzed ITO-coated glass plate was used as anode. The ITO electrode was washed with diluted ammonia, ethanol and water respectively. The two electrodes, placed parallel to each other with separation of 1 cm, were dipped in the colloidal suspension of SnO_2. The film deposition was carried out ITO plate (0.25 cm^2) at 40 mV for 30 s. the film were then removed from the suspension followed by washing with DI water to remove any unbound particles.

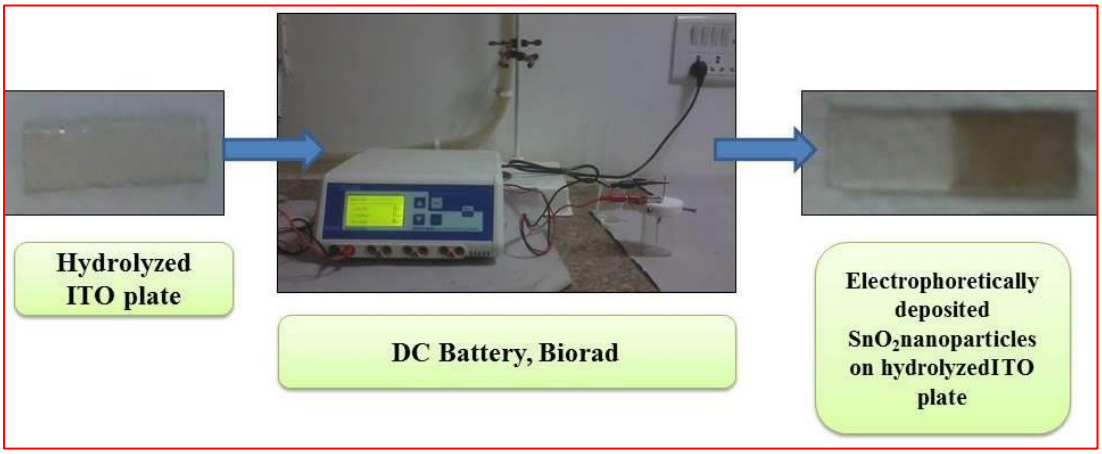

Figure 2.4: Electrophoretic deposition of SnO_2 nanoparticles on ITO electrode

2.3.4 Preparation of phosphate buffer solution

Phosphate buffer solution was prepared by mixing of two freshly prepared solutions, solution-**A** and solution-**B**. Solution-**A** was prepared by dissolving 6 g of monobasic sodium phosphate (sodium di-hydrogen phosphate, NaH_2PO_4) in 250 ml of de-ionized water and Solution-**B** was prepared by dissolving 7.1 g of dibasic sodium phosphate (disodium hydrogen phosphate, Na_2HPO_4) in 250 ml of de-ionized water.

Now the phosphate buffer solution of different pH can be obtained by mixing different proportion of solution-**A** and solution-**B** (X ml of Solution-**A** + Y ml of solution-**B**, diluted to a total of 200ml).

For pH 7: (39 ml of solution-A + 61 ml of solution-B) + 100 ml of DI water

For pH 5.7: (93.5 ml of solution-**A** + 6.5 ml of solution-**B**) + 100 ml of DI water

For pH 6.4: (73.5 ml of solution-**A** + 26.5 ml of solution-**B**) + 100 ml of DI water

For pH 7.5: (16ml of solution-**A** + 84ml of solution-**B**) + 100ml of DI water

For pH 8: (5.3ml of solution-**A** + 94.7ml of solution-**B**) + 100ml of DI water

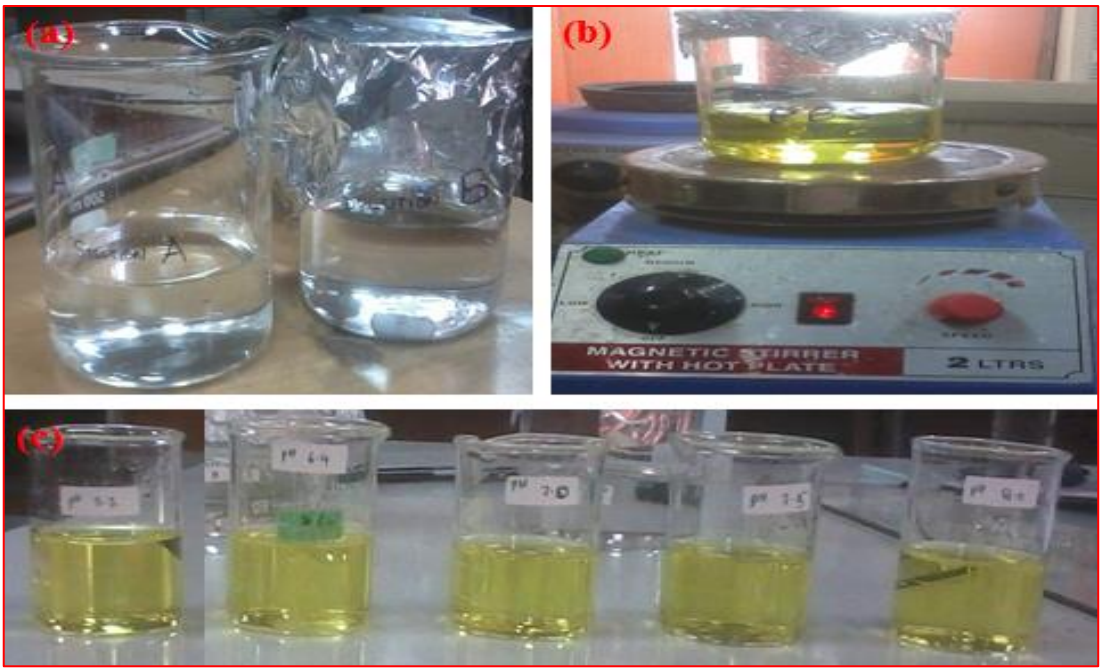

Figure 2.5: (a) Preparation of A & B solution, (b) Preparation of PBS solution, and (c) PB saline solution for 5 different pH (5.7, 6.4, 7, 7.5 and 8)

2.3.5 Preparation of phosphate buffer saline (PBS) solution

Phosphate buffer saline (PBS) solution was prepared by the addition of 0.9% of NaCl salt per 200 ml of phosphate buffer solution. Now 0.422 g of potassium ferrocyanide $\{K_4Fe(CN)_6\}$ and 0.329 g of potassium ferricyanide $\{K_3Fe(CN)_6\}$ were added to the PBS as mediator and shake well until it became yellowish clear solution. PBS solution was usually stored under refrigerated condition (4 ℃) when not in use.

2.3.6 Preparation of guar gum solution

Guar gum films are generally brittle in nature. Hence, to avoid the brittleness the guar gum solution was blended with polyvinyl alcohol. For the preparation of 1% (v/v) solution, 0.5 g of guar gum powder was added into 50 ml distilled water and kept for continuous stirring till it dissolves completely (~12 h). Simultaneously, 1% PVA solution was prepared in hot distilled water and then cooled at room temperature. Now, the PVA solution was added slowly to the guar

gum solution and the mixture was kept under constant stirring for overnight (12 h) on a magnetic stirrer at room temperature to get a homogeneous solution. This solution was further used in guar gum film and nanocomposite preparation. The prepared solution was stirred at 4 °C for future use.

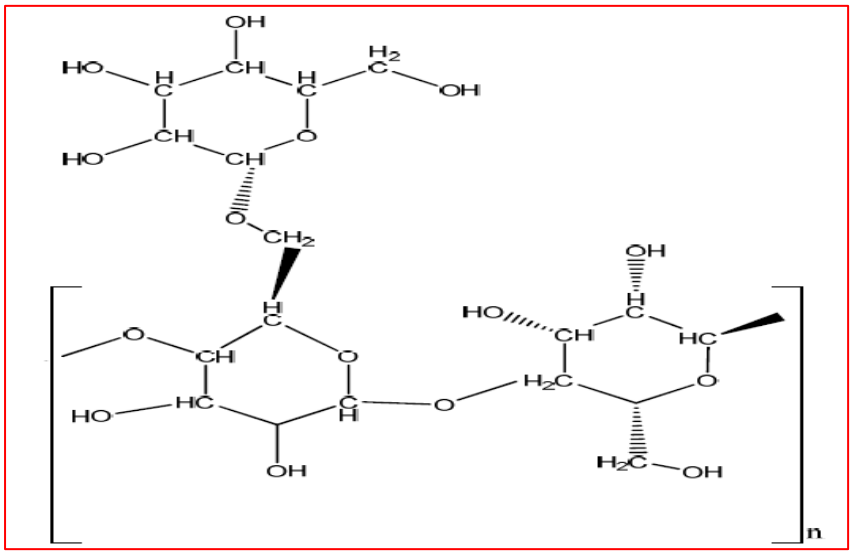

Figure 2.6: Chemical structure of guar gum

Figure 2.7: Preparation of guar gum solution

2.3.7 Preparation of SnO_2-GG nanocomposite film

30 mg of SnO_2 nanoparticles were dispersed into 5 ml of GG solution with stirring at room temperature followed by sonication for about 2 h to get a viscous GG solution with uniformly dispersed SnO_2 nanoparticles. The nanocomposite thin films were fabricated by uniformly spreading 10 µl solution of SnO_2-GG nanocomposite onto a functionalized ITO-coated glass surface (0.25 cm^2) and dried for 12 h at room temperature in a controlled environment and then washed with de-ionized water to remove any unbound particles.

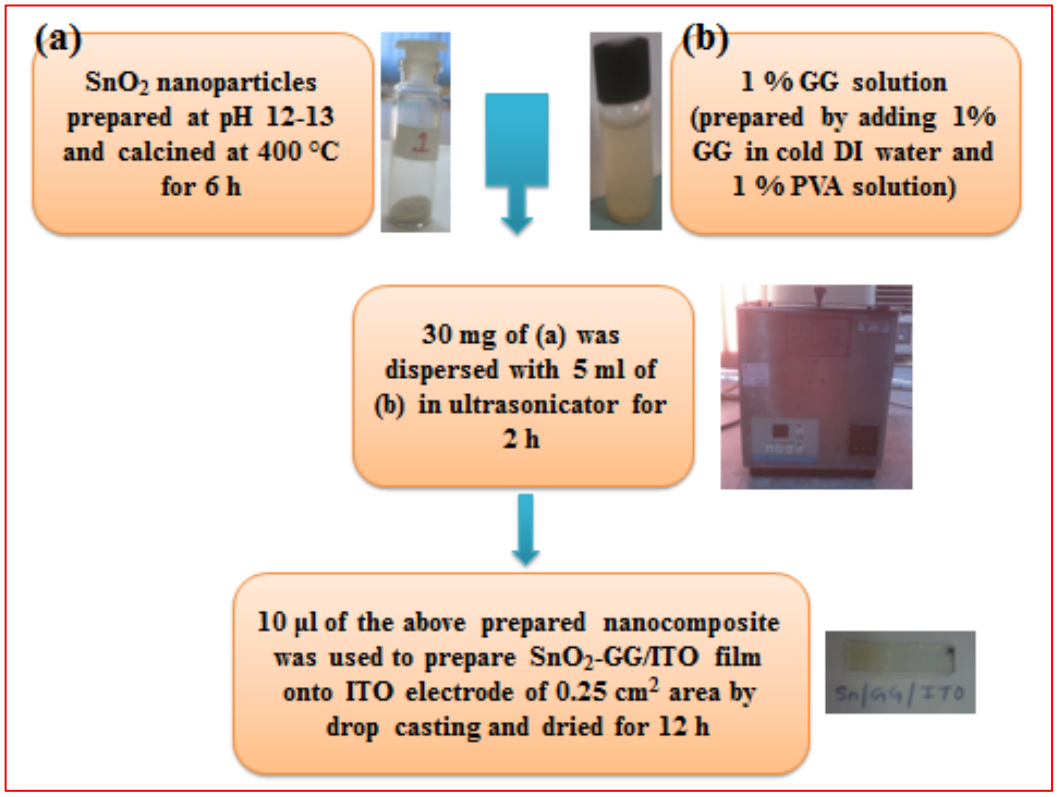

Figure: 2.8: Schematic representation of preparation of SnO_2-GG/ITO nanocomposite film

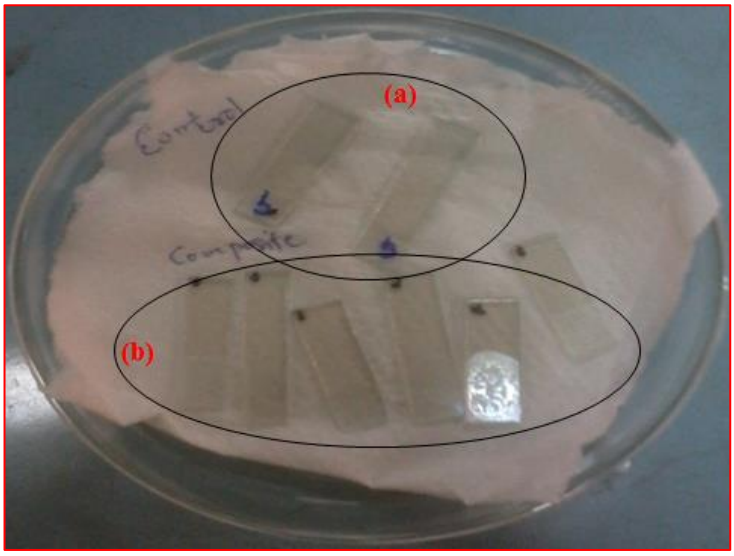

Figure 2.9: (a) GG/ITO and (b) SnO_2-GG/ITO nanocomposite electrode prepared by drop casting method

2.3.8 Preparation of hydrazine (N_2H_4) solution of different molarity

20.58 M solution of hydrazine (M_w = 50.06) was taken to prepare stock solutions of different molarity. Solutions of different working concentration of hydrazine (like 2, 5, 8, 12, 15, 20, and 22 mM) were prepared by serial dilution with de-ionized water.

Figure 2.10: Hydrazine solution of different molar concentrations

2.3.9 Antibacterial activity assay

2.3.9.1 Preparation of Nutrient Agar Media

Ingredients	**g/ l**
Peptone	5.000
Beef Extract	3.000
Agar	15.000

Preparation

28 g of nutrient agar was suspended in l000 ml distilled water. The mixture was heated to make it boil so as to dissolve the medium completely. It was then sterilized by autoclaving at 15 psi pressure (121°C) for 15 minutes. The contents were mixed well before dispensing.

2.3.9.2 Antibacterial activity test

The antibacterial activity of the synthesized SnO_2 nanoparticles, GG, and the SnO_2-GG nanocomposite was evaluated by swabbing method against *B. cereus* and *P. aeruginosa*. First of all, nutrient agar media was prepared in the autoclave at 121°C at 15 psi. After release of pressure from the autoclave, the media was poured aseptically into the petri plates in laminar air flow. The plates were allowed to cool down inside the laminar air flow so as to solidify the agar. After that bacterial colonies were picked from the sub cultured bacterial plates with the help of autoclaved cotton swabs. The cotton swab was dipped into autoclaved normal saline solution (0.9% NaCl solution) and then used to pick the bacterial colony. The swab was rubbed into the respective agar plate thoroughly at 360°. The agar plates were kept still for 10 min so that the bacterial culture gets little absorbed into the media. Then the wells were created in the swabbed agar plate for 4 samples using autoclaved wire loop. 30-40 µl samples were added into the respective wells in desired concentrations. A concentration dependent study was done for the SnO_2-GG nanocomposite; hence two samples for the nanocomposite were taken in 1 mg/ml and 0.25 mg/ml concentration. SnO_2 nanoparticles and GG were taken in 1 mg/ml concentration. The same steps were performed for testing antibacterial activity against both *B. cereus* and *P. aeruginosa*. Now, both the bacterial plates with loaded wells were incubated at 37 °C +/- 2 °C

for 24 h in BOD incubator. Next day the respective values of the inhibition zones formed were collected.

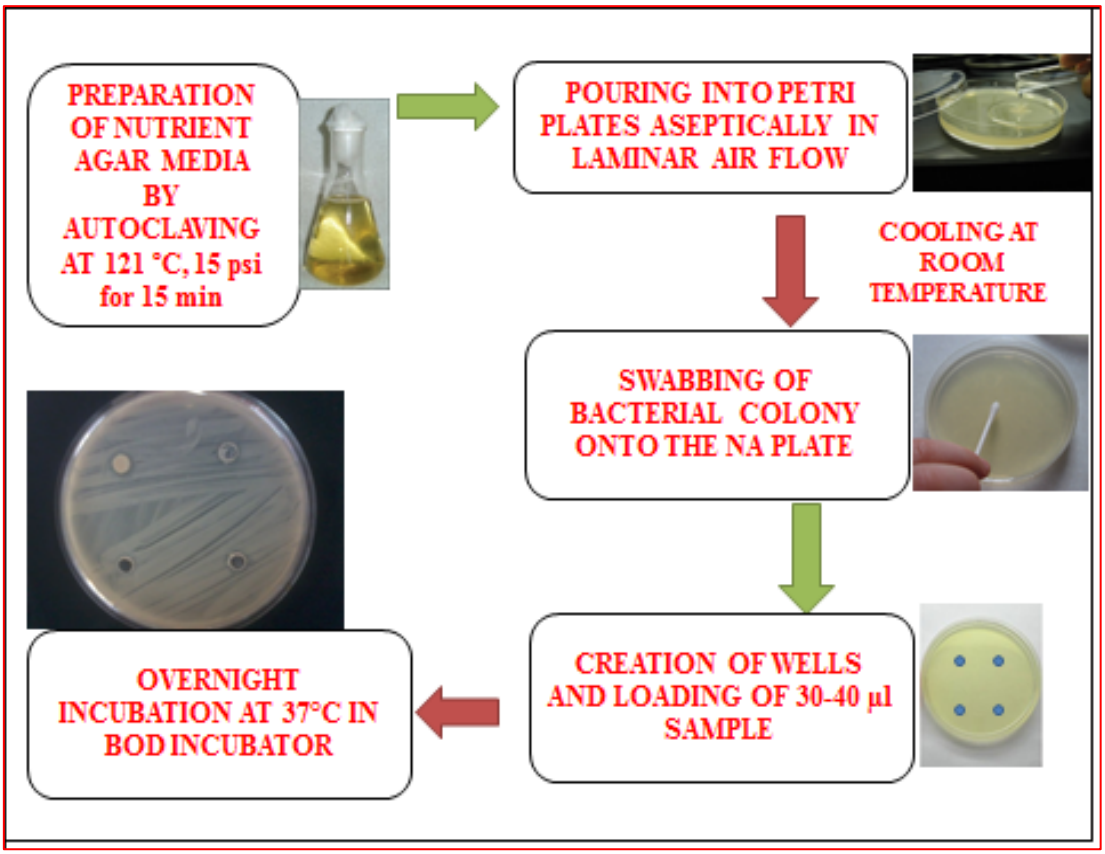

Figure 2.11: Schematic representation of antibacterial activity assay

2.4 Characterization techniques

2.4.1 X-ray Diffraction (XRD)

X-ray powder diffraction (XRD) is utilized for determination of polymorphism in crystalline organic materials. The stability of organic materials is an important issue in the manufacture and performance of imaging materials and devices. A common problem that exists in organic materials is polymorphism. Polymorphism is the ability of a singular molecular species to crystallize in more than one crystal structure. These multiple crystal structures are the result of different packing configurations of the molecule in a crystal. Pseudo-polymorphism is a variant of polymorphism, where a solvent molecule(s) is part of the lattice resulting in a crystal structure change. As a means of understanding the presence or absence of polymorphism in organics, X-ray diffraction (XRD) is now routinely used as the method of choice for identifying these crystal phase modifications. It is important to note that if a material is amorphous, XRD may provide minimal information related to polymorphism. [34]

X-ray diffraction (XRD) is a powerful method for the study of nanomaterials (materials with structural features of at least one dimension in the range of 1-100 nm). The wavelength of X-rays is on the atomic scale, so X-ray diffraction (XRD) is a primary tool for probing structure of nano-materials [35].

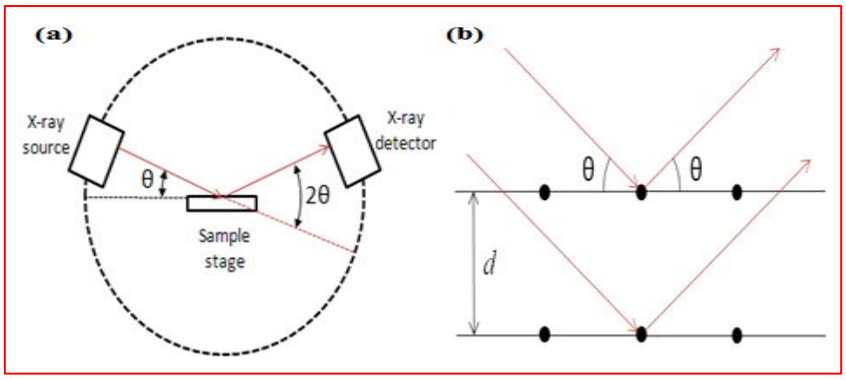

Figure 2.12: Schematic representation of (a) basic features of X-ray diffractometer and (b) Bragg's law

The lattice planes in the simple crystal in Figure b are separated by a distance d. The Bragg's law relates the wavelength (λ) of the reflected X-ray, the spacing between the atomic planes (d) and the angle of diffraction (θ) as follows:

$$2d \sin\theta = n \lambda \qquad \text{……………………………………… (2.1)}$$

The angle between the transmitted and diffracted beams will always be equal to 2θ. This angle can be obtained readily in experimental situations and the results of X-ray diffraction are therefore given in terms of 2θ. It is however very important to remember that the angle that is used in the Bragg's equation must correspond to the angle between the incident radiation and the diffracting plane, i.e. θ. [36]. For the first order diffraction, n = 1, and knowing θ and λ, one can calculate the interplanar spacing d–value for a particular plane. The first step of X-ray diffraction pattern involves the indexing of XRD peaks. The indexing means assigning the correct Miller indices to each peak of the diffraction pattern. There are three main methods for indexing a diffraction pattern, (i) comparing the measured XRD pattern with the standard data base (JCPDS-cards) (ii) analytical methods (iii) graphical methods. The intensity of the diffraction signal is usually plotted against the diffraction angle 2 θ [°], but d [nm] or 1/d [nm^{-1}] may also be used. The most common wavelength used in XRD is 1.54 Å (Cu Kα). The line broadening can be a measure of the average size of the crystallites by using the Scherrer formula (2).

$$D_v = K \lambda / \beta \cos\theta \qquad \text{………………………………………… (2.2)}$$

Where; D_v is the average particle size, λ is wave length of the radiation and β is the FWHM (full width at half maximum) of the reflection peak that has the same maximum intensity in the diffraction pattern (integral breadth of the peak located at angle θ). K is the Scherrer constant. The Scherrer constant (K) in the formula accounts for the shape of the particle and is generally taken to have the value 0.9. The size obtained from the Scherrer formula yields the apparent or average particle-size for a material. Powders of materials are generally aggregates of smaller particles, and thus consist of a distribution of particle sizes.

XRD studies for this project have been carried out using Bruker D8 Advance Diffractometer with Ni-filtered Cu Kα radiation (IIT, New Delhi) with Voltage- 30 kV, 35 mA.

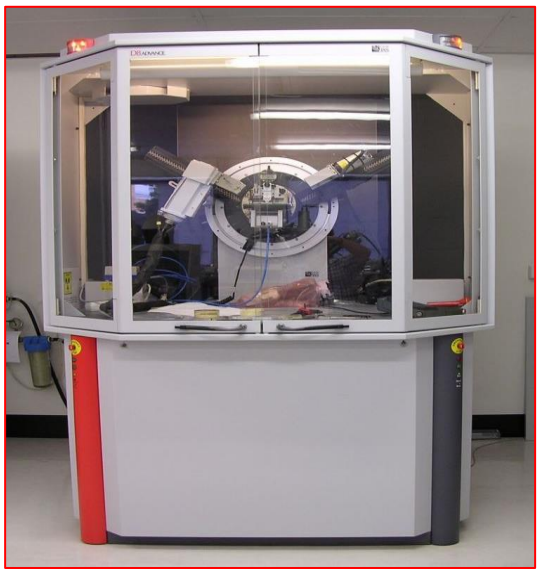

Figure 2.13: X-ray diffraction machine.

2.4.2 Fourier transform infrared (FT-IR) spectroscopy

FTIR spectroscopy is a powerful technique for studying the molecular orientation and ordering. Infrared (IR) spectroscopy detects the vibration characteristics of chemical functional group in a sample. When an IR radiation is passed through a sample, some of the infrared radiation is absorbed by the sample and some of it is passed through or transmitted. The resulting spectrum represents the molecular absorption and transmission, creating a molecular fingerprint of the sample. There are two kinds of fundamental vibrations for molecules: *stretching*, in which the distance between two atoms increases or decreases, but the atoms remain in the same bond axis, and *bending* or deformation, in which the position of the atom changes relative to the original bond axis. The various stretching and bending vibrations of a bond occur at certain quantized frequencies. When infrared light of that same frequency is incident on the molecule, energy is absorbed and the amplitude of that vibration is increased. When the molecule reverts from the excited state to the original ground state, the absorbed energy is released as heat [37-38]. So after interaction of IR light with the material, chemical bonds will stretch, contract and

bend. As a result, a chemical functional group tends to adsorb IR in a specific wavenumber range regardless of the structure of rest of the molecule. For example, the C=O stretch of a carbonyl group appears at around 1700cm^{-1} in a variety of molecules. Hence, the correlation of the bond and wavenumber position with the chemical structure is used to identify a functional group in a sample.

A beam splitter divides laser light entering the input port into a transmitted beam and a reflected beam, perpendicular to each other. At the end of each beam's path, a mirror reflects the light back toward the beam splitter. If the two beams' paths have exactly the same length, the beams' electric fields oscillate in phase when the light returns to the beam splitter. The beams recombine to produce a beam that exits the beam splitter along the output port. If the two paths differ in length by half a wavelength, they are out of phase. In that case, they interfere destructively at the beam splitter and no light exits from the output port. The intensity of light leaving the output port changes from a maximum to zero as the relative distance to the end mirrors changes by a quarter of a wavelength—about 2.5 x 10^{-7} m for typical laser light. Precisely measuring this light intensity allows experimenters to detect even smaller relative displacements of the mirrors. Any passing gravitational wave should compress space-time in one direction and stretch it out in the perpendicular direction. [39]

FTIR studies for this project have been carried out using Thermoscientific Nicolet 380 (DTU, Delhi).

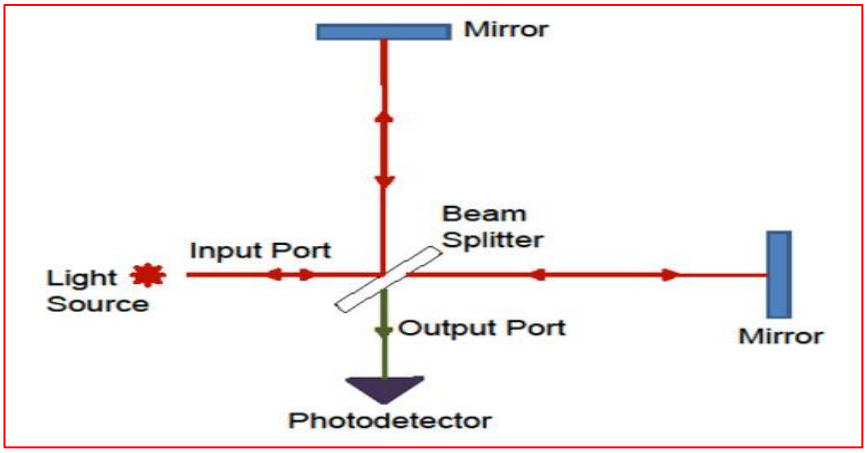

Figure 2.14: Schematic diagram showing working of FTIR spectrophotometer

Figure 2.15: Thermoscientific Nicolet 380 at DTU, Delhi

2.4.3 Scanning Electron Microscopy (SEM)

A normal scanning electron microscope operates at a high vacuum. The basic principle is that a beam of electrons is generated by a suitable source, typically a tungsten filament or a field emission gun. The electron beam is accelerated through a high voltage (e.g.: 20 kV) and pass through a system of apertures and electromagnetic lenses to produce a thin beam of electrons, then the beam scans the surface of the specimen by means of scan coils (like the spot in a cathode-ray tube "old-style" television).

Electrons are emitted from the specimen by the action of the scanning beam and collected by a suitably-positioned detector. The microscope operator is watching the image on a screen. Imagine a spot on the screen scanning across the screen from left to right. At the end of the screen, it drops down a line and scans across again, the process being repeated down to the bottom of the screen.

The key to how the scanning electron microscope works is that the beam scanning the specimen surface is *exactly* synchronized with the spot in the screen that the operator is

watching. The electron detector controls the brightness of the spot on the screen - as the detector "sees" more electrons from a particular feature, the screen brightness is increased. When there are fewer electrons, the spot on the screen gets darker. These days, the screen used is generally a digital monitor.

The magnification of the image is the ratio of the size of the screen to the size of the area scanned on the specimen. If the screen is 300 mm across and the scanned area on the specimen is 3 mm across, the magnification is x 100. To go to a higher magnification, the operator scans a smaller area; if the scanned area is 0.3 mm across, the magnification is x 1000, and so on.

There are different types of electron image. The two most common are the secondary electron image (*sei*) and the backscattered electron image (*bei*). The *sei* is used mainly to image fracture surfaces and gives a high resolution image. The *bei* is used typically to image a polished section; the brightness of the *bei* is dependent on the atomic number of the specimen (or, for compounds, the average atomic number). For example, lead will appear brighter than iron and calcium oxide will appear brighter than calcium carbonate. The *bei* is, in essence, an atomic number map of the specimen surface. All SEM images are in black-and-white, although they may subsequently have false colors applied to them for aesthetic reasons or to aid interpretation.

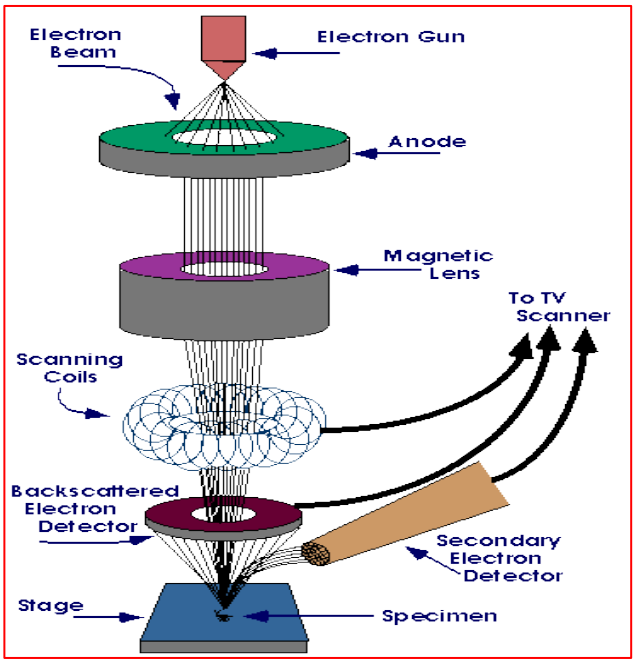

Figure 2.16: Schematic representation of components of SEM

2.4.3.1 Energy-dispersive X-ray microanalysis (EDX)

Energy-dispersive X-ray microanalysis (EDX) is complementary to SEM. It enables the operator to determine the composition of the features in the SEM image. The principle of EDX is that the electron beam generates X-rays within the specimen. Many of these X-rays have energies characteristic of the elements that emitted them. So, if you can measure the energy of the X-rays, you know what elements are present in the specimen. If you control the instrumental conditions carefully you can determine not only what elements are present but their concentrations.

There are three principal components to a basic EDX system: the X-ray detector; a box of electronics called the "pulse processor" that measures the voltage pulses corresponding to the X-ray energies, and a computer, typically a PC. The X-ray detector is positioned to intercept X-rays emitted from the specimen. On entering the detector, an X-ray generates a small current, which is then converted into a voltage pulse. The size of the voltage pulse is proportional to the energy of the X-ray. A computer measures the voltage pulses over a period of time, says 60 s and plots them as a histogram. The histogram shows a spectrum of the X-ray energies that were measured; by examining the spectrum, the elements present can be determined. The EDX system may also be able to take control of the SEM scanning system in order to collect elemental distribution maps ("dot maps") or elemental line profiles.

The SEM and EDX studies for this project have been done using HITACHI, Model No.S-3700N with EDS-X with X-ray (DTU, Delhi).

Figure 2.17: SEM HITACHI, Model No.S-3700N with EDS-X with X-ray at DTU, Delhi

2.4.4 Transmission electron microscopy (TEM)

Transmission Electron Microscopy (TEM) is a vital characterization tool for directly imaging nanomaterials to obtain quantitative measures of particle and/or grain size, size distribution, and morphology. TEM images the transmission of a focused beam of electrons through a sample, forming an image in an analogous way to a light microscope. However, because electrons are used rather than light to illuminate the sample, TEM imaging has significantly higher resolution (by a factor of about 1000) than light -based imaging techniques. Amplitude and phase variations in the transmitted beam provide imaging contrast that is a function of the sample thickness (the amount of material that the electron beam must pass through) and the sample material (heavier atoms scatter more electrons and therefore have a smaller electron mean free path than lighter atoms).

Successful imaging of nanoparticles using TEM depends on the contrast of the sample relative to the background. Samples are prepared for imaging by drying nanoparticles on a copper grid that is coated with a thin layer of carbon. Materials with electron densities that are significantly higher than amorphous carbon are easily imaged. These materials include most metals (e.g., silver, gold, copper, aluminum), most oxides (e.g., silica, aluminum oxide, titanium oxide), and other particles such as polymer nanoparticles, carbon nanotubes, quantum dots, and magnetic nanoparticles.

Figure 2.18: TEM copper grid dipped and dried with the naonoparticle sample

Figure 2.19: TEM machine at AIIMS, New Delhi

The transmission electron microscope (TEM) forms an image by accelerating a beam of electrons that pass through the specimen. In TEM, electrons are accelerated to 100 keV or higher (up to 1 MeV), projected onto a thin specimen (less than 200 nm) by means of the condenser lens system, and penetrate the sample thickness either undeflected or deflected. The greatest advantages that TEM offers are the high magnification ranging from 50 to 10^6 and its ability to provide both image and diffraction information from a single sample.

The scattering processes experienced by electrons during their passage through the specimen determine the kind of information obtained. Elastic scattering involves no energy loss and gives rise to diffraction patterns. Inelastic interactions between primary electrons and sample electrons at heterogeneities such as grain boundaries, dislocations, second phase particles, defects, density variations, etc., cause complex absorption and scattering effects, leading to a spatial variation in the intensity of the transmitted electrons. In TEM one can switch between imaging the sample and viewing its diffraction pattern by changing the strength of the intermediate lens. TEM studies have been done for this project with the help of FEI Tecnai S Twin (AIIMS, New Delhi).

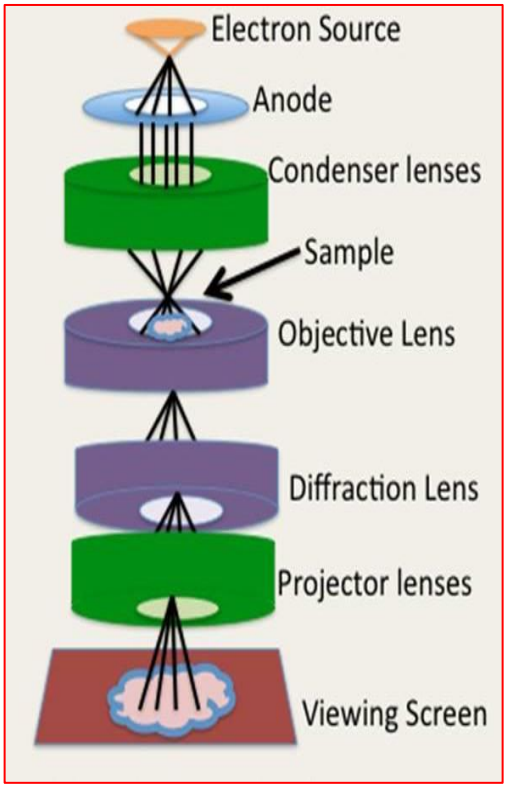

Figure 2.20: Pictorial view of main components of a TEM

2.4.5 Atomic Force Microscopy (AFM)

The atomic force microscope (AFM) is a very high-resolution type of scanning probe microscopy (SPM), with demonstrated resolution on the order of fractions of a nanometer, more than 1000 times better than the optical diffraction limit. SPMs are designed to measure local properties, such as height, friction, magnetism, with a probe. To acquire an image, the SPM raster scans the probe over a small area of the sample, measuring the local property simultaneously.

The atomic force microscope feels the surface of a sample with such a discriminating touch that it can sometimes even sense the individual atoms on the surface of a crystal such as gold. The AFM does this by raster-scanning a small tip back and forth over the sample surface. The tip is on the end of a cantilever, which deflects when the tip encounters features on the sample surface. This deflection is sensed with an optical lever (red line): a laser beam reflecting off the end of the cantilever onto a segmented photodiode magnifies small cantilever deflections into large changes in the relative intensity of the laser light on the two segments of the photodiode. In this way, the AFM makes a topographic map of the sample surface.

AFM imaging in contact mode can damage or distort some soft biological samples. Tapping Mode or Non-contact Mode minimizes this problem by having the tip oscillate over the sample, making only brief intermittent contacts. This mode also provides additional information about the sample surface in the phase image that corresponds to the height image.

AFM studies for this project have been done with Park Systems, XE 100 at DTU, Delhi.

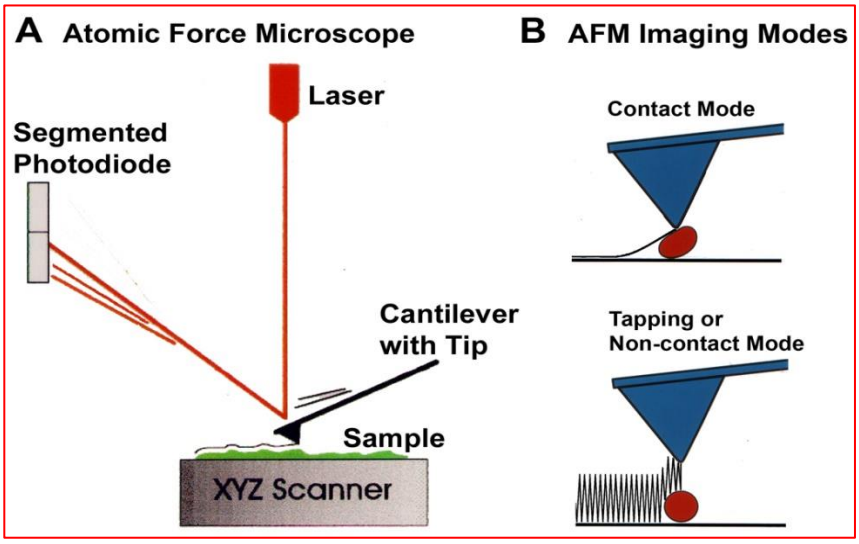

Figure 2.21: (a) Block diagram showing components of AFM and (b) AFM imaging modes

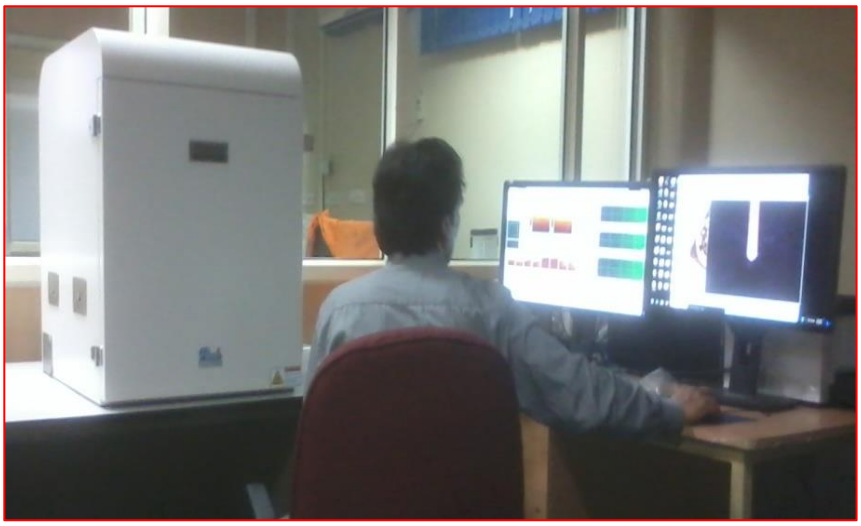

Figure 2.22: Park Systems XE-100 AFM at DTU, Delhi

2.4.6 UV-Vis Spectroscopy

Absorption in the ultraviolet (UV) and visible (vis) region of the spectrum is an important technique of analysis and is dependent on the electronic structure of the molecule [40]. This is an excellent tool for detection and for determining the concentration of a compound which absorbs the energy in the UV-visible region.

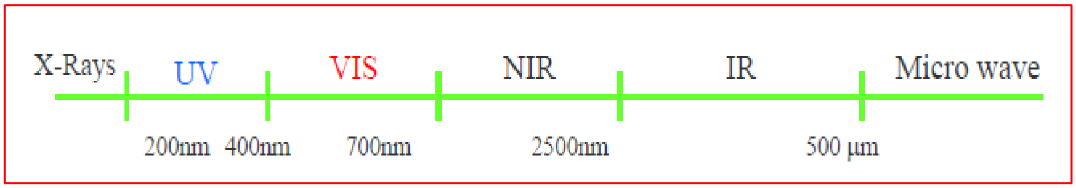

Figure 2.23: Range of electromagnetic spectrum

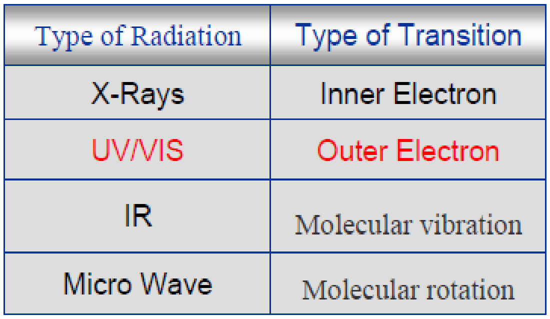

Type of Radiation	Type of Transition
X-Rays	Inner Electron
UV/VIS	Outer Electron
IR	Molecular vibration
Micro Wave	Molecular rotation

Figure 2.24: Types of transitions in different types of radiations

According to the Beer's law, absorption is proportional to the number of absorbing molecules i.e. to the concentration of absorbing molecules (true for only dilute solutions), and the Lambert's law says that the fraction of radiation absorbed is independent of the intensity of the radiation. Combining these two laws, Beer-Lambert law is derived as,

$$\log_{10} I_0/I = \varepsilon lc \qquad \ldots\ldots\ldots\ldots\ldots\ldots\ldots\ldots\ldots\ldots \text{(2.3)}$$

where, I_0 = Intensity of the incident radiation,

I = Intensity of the transmitted radiation,

ε = molar absorption coefficient ($mol^{-1}dm^{3}cm^{-1}$)

l = path length of the absorbing solution in cm

c = concentration of the absorbing species in $moldm^{-3}$

The value of $\log_{10} I_0/I$ is known as the absorbance of the solution, and can be read directly from the spectrum, often as 'absorbance units'. A useful constant is the molar absorption coefficient, ε, because it is independent of concentration and path length, whereas absorption

depends upon both. The other useful piece of information is the wavelength at which maximum absorption occurs. This is given the symbol λ_{max}.

UV/Vis involves the spectroscopy of photons in the UV-visible region. This means it uses light in the visible and adjacent (near ultraviolet (UV) and near infrared (NIR)) ranges. The absorption in the visible ranges directly affects the color of the chemicals involved. In this region of the electromagnetic spectrum, molecules undergo electronic transitions. This technique is complementary to fluorescence spectroscopy, in that fluorescence deals with transitions from the excited state to the ground state, while absorption measures transitions from the ground state to the excited state. In sunlight (white light) as uniform or homogeneous in colour, it is actually composed of a broad range of radiation wavelengths in the ultraviolet (UV), visible and infrared (IR) portions of the spectrum. Electromagnetic radiation such as visible light is commonly treated as a wave phenomenon, characterized by a wavelength or frequency. Wavelength is defined as the distance between adjacent peaks (or troughs), and may be designated in m, cm or nm (10^{-9} m). The wavelengths of what we perceive as particular colours in the visible portion of the spectrum are displayed and listed below.

- Violet: 400 - 420 nm
- Indigo: 420 - 440 nm
- Blue: 440 - 490 nm
- Green: 490 - 570 nm
- Yellow: 570 - 585 nm
- Orange: 585 - 620 nm
- Red: 620 - 780 nm

When sample molecules are exposed to light having an energy that matches a possible electronic transition within the molecule, some of the light energy will be absorbed as the electron is promoted to a higher energy orbital. An optical spectrometer records the wavelengths

at which absorption occurs, together with the degree of absorption at each wavelength. The resulting spectrum is presented as a graph of absorbance (A) versus wavelength.

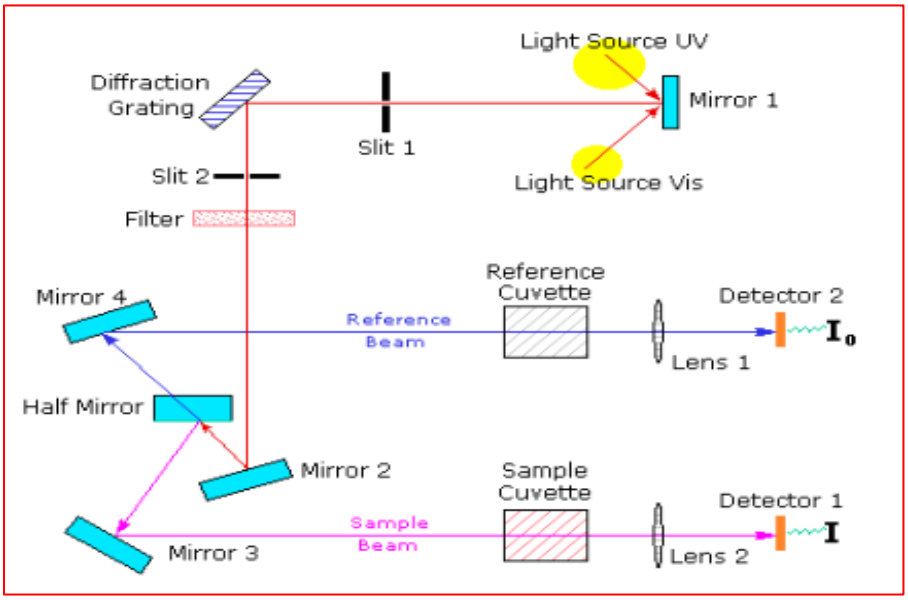

Figure 2.25: Schematic diagram showing main components of UV-Vis spectrophotometer

The UV-Visible spectrophotometer uses two light sources, a deuterium lamp for ultraviolet light and a tungsten lamp for visible light. After bouncing off a mirror (mirror 1), the light beam passes through a slit and hits a diffraction grating. The grating can be rotated allowing for a specific wavelength to be selected. At any specific orientation of the grating, only monochromatic successfully passes through a slit. A filter is used to remove unwanted higher orders of diffraction. One of the beams is allowed to pass through a reference cuvette, the other passes through the sample cuvette. The intensities of the light beams are then measured at the end.

UV-vis studies in this project have been done with UV/VIS/NIR spectrometer PerkinElmer, Lambda 950, DTU, Delhi.

Figure 2.26: PerkinElmer, Lambda 950 UV-Vis Spectrophotometer at DTU, Delhi

2.4.7 Photoluminescence (PL) Spectroscopy

Photoluminescence is a method for probing the electronic structure of materials in a contactless and non-destructive way. In a process called photo-excitation, light is directed onto the sample, where it is absorbed and excess energy is imparted to the material. This energy can be dissipated by the sample in the form of emission of light, called luminescence. When photo-excitation takes place this luminescence is called photoluminescence.

There are many forms of PL, one is resonant radiation. In this method, a photon of a specific wavelength is absorbed and an equivalent photon is immediately emitted out, hence no significant energy transitions are involved between absorption and emission. The process is usually of the order of 10 ns. In case of fluorescence, the chemical substrate undergoes energy transitions before coming back to its ground state by emitting photons; some of the absorbed energy is dissipated out so that the emitting electrons are of lower energy than the absorbed ones. This phenomenon has a shorter lifetime (10^{-8} to 10^{-4} s). Phosphorescence is a radiational transition, in which the absorbed energy undergoes intersystem crossing into a state with a different spin multiplicity. The lifetime of phosphorescence is usually from 10^{-4} - 10^{-2} s, much longer than that of Fluorescence.

The basic elements of a PL spectroscopy set-up consist in an optical source, a spectrophotometer and a detector. A typical PL set-up is shown in Fig 2.14. The excitation laser beam is focused on the sample with a lens of typically f = 20-30 cm focal length. The emitted light can be collected by a single lens (2f/2f geometry) or by two lenses F_1 and F_2. The advantage of this latter geometry is to allow the use of a short focal length for F_1 in order to improve the collection efficiency of the emitted light. Moreover, F_2 can be chosen in order to match the optical aperture of the spectrometer, avoiding unnecessary supplementary losses. [41]

PL studies for this project have been carried out using Fluorolog 3 (made by Horiba) at DTU, Delhi.

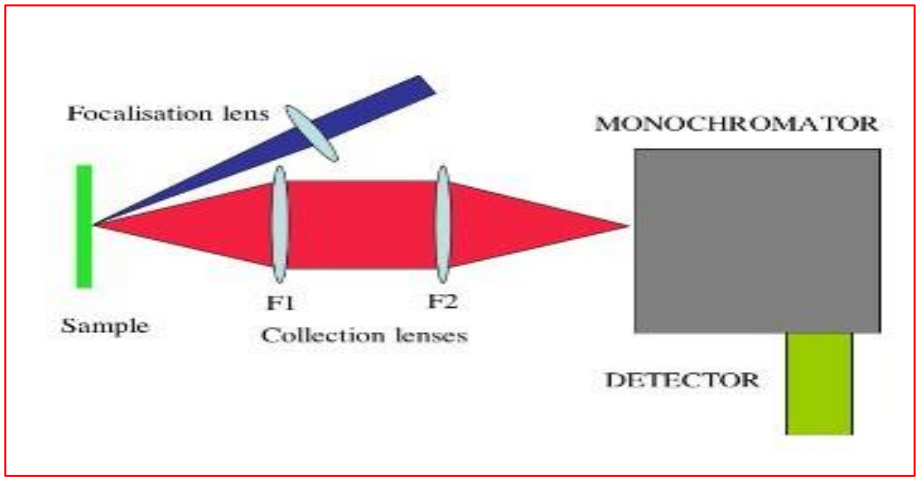

Figure 2.27: Block diagram showing main components of PL spectrophotometer

Figure 2.28: PL spectroscopy machine

2.4.8 Electrochemical techniques

Electrochemical techniques are powerful and versatile analytical techniques that offer high sensitivity, accuracy, and precision as well as large linear dynamic range, with relatively low-cost instrumentation. After developing more sensitive pulse methods, the electroanalytical studies are more regularly used on industrial, environmental applications and on the drug analysis in their dosage forms and especially in biological samples. However, electroanalytical techniques can easily solve many problems of pharmaceutical interest with a high degree of accuracy, precision, sensitivity, and selectivity employing this approach [42]. Electrochemistry is the study of the chemical response of a system to an electrical stimulation. The scientist using electrochemistry studies the loss of electrons (oxidation) or gain of electrons (reduction) that a material undergoes during the electrical stimulation. These reduction and oxidation reactions are commonly known as redox reactions and can provide information about the concentration, kinetics, reaction mechanisms, chemical status and other behavior of a species in solution. Similar information can be obtained concerning the electrode surface. Electrochemical techniques can be used to investigate many things – from neurotransmitter behavior in biological situations to brightener concentrations in plating baths to initiator behavior in polymerizations to the speciation of cadmium ions in natural waters.

In an electrochemical experiment, we can measure one or more of four parameters – potential (E), current (i), charge (Q) and time (t). The response of a system depends on which parameter is used as the excitation signal. By plotting different parameters in different ways, we can derive a wealth of information. Most of the electrochemical techniques involves three electrodes – the working electrode, the reference electrode and the counter (or auxiliary) electrode. The three electrodes are connected to a potentiostat, an instrument which controls the potential of the working electrode and measures the resulting current. In one typical electrochemical experiment, a potential is applied to the working electrode and the resulting current measured then plotted versus time. In another, the potential is varied and the resulting current is plotted versus the applied potential [43].

The different combinations of parameters and working electrode types make for a long list of techniques as follows:

- Voltammetry
- Polarography
- Cyclic voltammetry
- Linear sweep techniques
- Chronoamperometry
- Chronopotentiometry
- Pulsed techniques

2.4.8.1 Cyclic Voltammetry

Cyclic voltammetry (CV), one of the more commonly used electroanalytical techniques, is an excellent methods development tool. Its main advantage in electroanalysis is its ability to characterize an electrochemical system. A single CV experiment only hints at the events that constitute the electrochemical reaction at the electrode. However, multiple CV experiments can be used for a variety of applications, including:

- the determination of Nernstian (reversible) or non- Nernstian (irreversible) behavior of a redox couple
- the number of electrons transferred in an oxidation or reduction
- formal potentials
- rate constants
- formation constants
- reaction mechanisms
- diffusion coefficients

The potential of the working electrode is measured against a reference electrode which maintains a constant potential, and the resulting applied potential produces an excitation signal such as that of Fig 2.29 [44] In the forward scan of Figure 2.29, the potential first scans negatively, starting from a greater potential (a) and ending at a lower potential (d). The potential

extrema (d) is call the switching potential, and is the point where the voltage is sufficient enough to have caused an oxidation or reduction of an analyte. The reverse scan occurs from (d) to (g), and is where the potential scans positively. Fig 2.29 shows a typical reduction occurring from (a) to (d) and an oxidation occurring from (d) to (g). It is important to note that some analytes undergo oxidation first, in which case the potential would first scan positively. This cycle can be repeated, and the scan rate can be varied. The slope of the excitation signal gives the scan rate used.

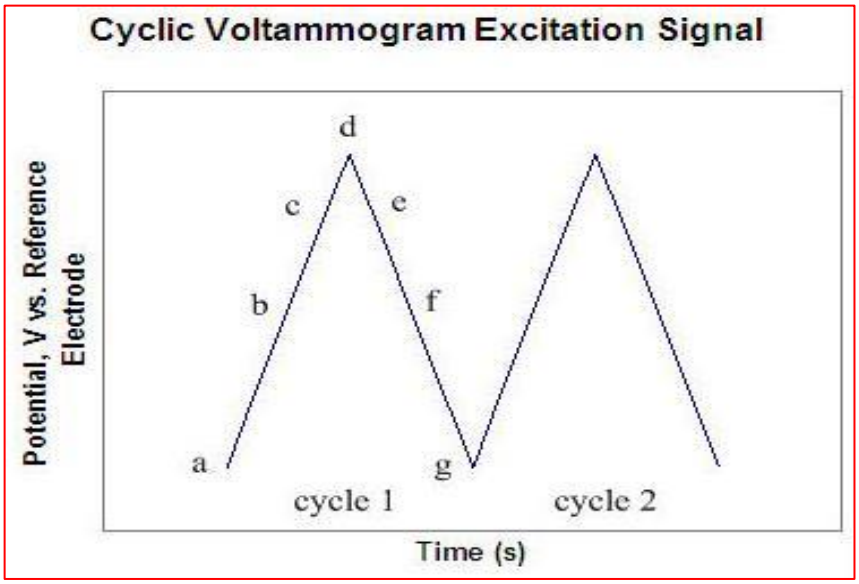

Figure 2.29: Graphical representation of cyclic voltammogram excitation signal

A cyclic voltammogram is obtained by measuring the current at the working electrode during the potential scans [44]. Fig 2.30 shows a cyclic voltammogram resulting from a single electron reduction and oxidation. Consider the following reversible reaction:

$$M^{+} + e^{-} \rightleftharpoons M \qquad \text{.....(2.4)}$$

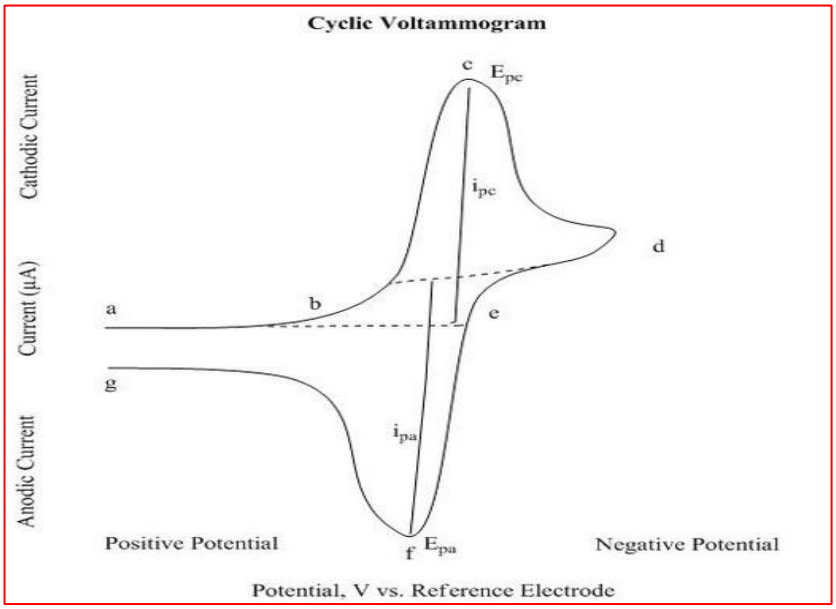

Figure 2.30: Cyclic voltammogram of a single electron oxidation-reduction

In Fig 2.30, the reduction process occurs from (a) the initial potential to (d) the switching potential. In this region the potential is scanned negatively to cause a reduction. The resulting current is called cathodic current (i_{pc}). The corresponding peak potential occurs at (c), and is called the cathodic peak potential (E_{pc}). The E_{pc} is reached when all of the substrate at the surface of the electrode has been reduced. After the switching potential has been reached (d), the potential scans positively from (d) to (g). This results in anodic current (I_{pa}) and oxidation to occur. The peak potential at (f) is called the anodic peak potential (E_{pa}), and is reached when all of the substrate at the surface of the electrode has been oxidized.

2.4.8.1.1 Useful Equations for Reversible Systems

Electrode potential (E):

$$E = E_i + vt \qquad \ldots\ldots\ldots\ldots\ldots\ldots\ldots\ldots\ldots\ldots\ldots\ldots\ldots\ldots \quad (2.5)$$

where (E_i) is the initial potential in V,

(v) is the sweep rate in Vs^{-1}, and t is the time in s

When the direction of the potential sweep is switched, the equation becomes,

$$E = E_s - vt \qquad \ldots\ldots\ldots\ldots\ldots\ldots\ldots\ldots\ldots\ldots\ldots\ldots \quad (2.6)$$

Where (E_s) is the potential at the switching point.

Electron stoichiometry (n):

$$E_p - E_{p/2} > 0.0565n \qquad \ldots\ldots\ldots\ldots\ldots\ldots\ldots\ldots\ldots\ldots\ldots\ldots \quad (2.7)$$

Where (E_{pa}) is the anodic peak potential, (E_{pc}) is the cathodic peak potential, and (n) is the number of electrons participating in the redox reactions.

Formal Reduction Potential (E°') is the mean of the E_{pc} and E_{pa} values:

$$E°' = (E_{pa} + E_{pc})/2 \qquad \ldots\ldots\ldots\ldots\ldots\ldots\ldots\ldots\ldots\ldots\ldots\ldots \quad (2.8)$$

2.4.8.1.2 Instrumentation

A CV system consists of an electrolysis cell, a potentiostat, a current-to-voltage converter, and a data acquisition system. The electrolysis cell consists of a working electrode, counter electrode, reference electrode, and electrolytic solution. The working electrode's potential is varied linearly with time, while the reference electrode maintains a constant potential. The counter electrode conducts electricity from the signal source to the working electrode. The purpose of the electrolytic solution is to provide ions to the electrodes during oxidation and reduction. A potentiostat is an electronic device which uses a dc power source to produce a potential which can be maintained and accurately determined, while allowing small currents to be drawn into the system without changing the voltage. The current-to-voltage converter measures the resulting current, and the data acquisition system produces the resulting voltammogram.

2.4.8.1.3 Applications

Cyclic Voltammetry can be used to study qualitative information about electrochemical processes under various conditions, such as the presence of intermediates in oxidation-reduction reactions, the reversibility of a reaction. CV can also be used to determine the electron stoichiometry of a system, the diffusion coefficient of an analyte, and the formal reduction potential, which can be used as an identification tool. In addition, because concentration is proportional to current in a reversible, Nernstian system, concentration of an unknown solution can be determined by generating a calibration curve of current vs. concentration.

Electrochemical studies for this project have been carried out with Metrohm Potentiostat/galvanostat at DTU, Delhi.

Figure 2.31: Metrohm Potentiostat/Galvanostat at DTU, Delhi

3. Results and discussion

This chapter describes the various results and information obtained during the characterization of SnO_2 nanoparticles and SnO_2-GG nanocomposite.

3.1Structural and Optical Characterization

3.1.1 X-ray diffraction study

The crystalline nature of SnO_2 formed in this study has been evaluated with the XRD pattern. The Fig 3.1 shows the XRD curves of GG (a), SnO_2 nanoparticles (b), and SnO_2-GG nanocomposite (c). The XRD data have been collected in the 2θ range of 10-80°. Fig 3.1(a) shows the XRD curve of GG. Two broad peaks are obtained for GG with 2θ values 19.75 and 40.77°, showing its amorphous nature. The XRD profile of the SnO_2-GG nanocomposite (figure (c) is in full agreement with the SnO_2 nanoparticles presented in Fig 3.1(b) that exhibits characteristic peaks at 2θ values of 26.57, 33.81, 51.80, 54.68, 57.74, 61.78, 65.71, 71.20 and 78.61° corresponding with scattering from the (1 1 0), (1 0 1), (2 1 1), (2 2 0), (0 0 2), (3 1 0), (3 0 1), (2 0 2) and (3 2 1) respectively. On matching the observed and standard (D_{hkl}) planes it is confirmed that the SnO_2 nanoparticles have a tetragonal structure in agreement with that of SnO_2 JCPDS No. 41-1445 [45].

The average particle size (D) was estimated using the Scherrer equation:

$$D = 0.9\,\lambda / \beta \cos\theta \qquad \text{…….....} \quad (3.1)$$

where D is the crystallite size, λ is the X-ray wavelength (1.5406 Å), β is the full width at half maximum of the most intense diffraction peak lying at plane (2 1 1) and θ is the Bragg diffraction angle of the diffraction peaks [21]. The average particle size for the SnO_2 nanoparticles is 10.6 nm, while the SnO_2-GG nanocomposite particles have an average particle size of ~17 nm. The X-ray diffraction curve of the nanocomposite shows similar peaks as that of the SnO_2 nanoparticles and the GG. Hence, Fig 3.1(c) confirms the synthesis of SnO_2-GG nanocomposite.

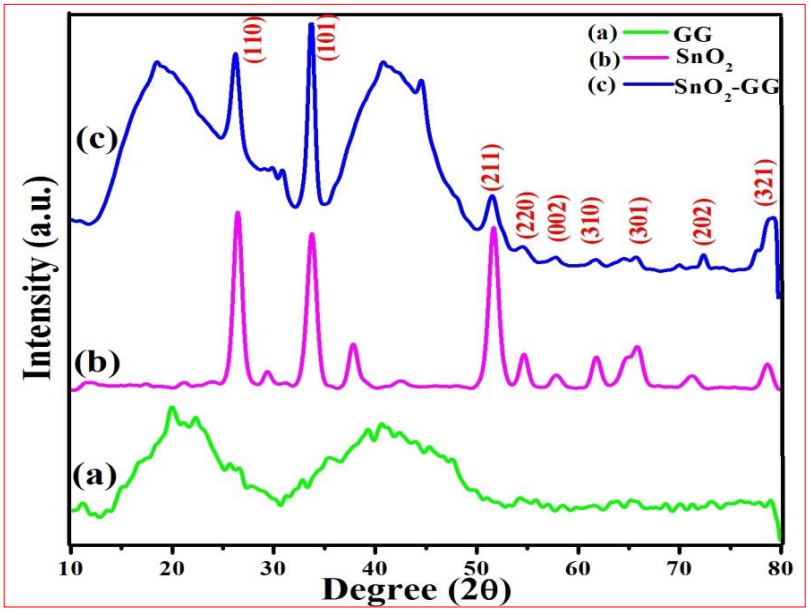

Figure 3.1: X-ray diffraction spectra of (a) GG, (b) SnO_2 nanoparticles and (c) SnO_2-GG nanocomposite

3.1.1 FT-IR Spectroscopy Study

The FTIR spectra of GG, nanostructured SnO_2 film and SnO_2-GG are shown in Fig 3.2(a), (b) and (c), respectively in the range of 4000-400 cm^{-1}. Fig 3.2(a) shows absorption bands at 3430 cm^{-1} associated with stretching vibrations of –OH. Peak at 2930 and 1430 cm^{-1} show the absorption band associated with the –CH bending vibration. Peak obtained at 1640 cm^{-1} corresponds to the bending vibration of –OH. The peak at 1020 cm^{-1} is associated with the stretching vibration of C-OH bond.

Fig 3.2(b) shows a broad band is obtained at 3430 cm^{-1} due to the stretching vibrations because of O-H groups or water molecules absorbed at the surface of SnO_2 sample. The peak at 1640 cm^{-1} is attributed to the bending vibration of water molecules that are trapped in SnO_2 nanoparticles. A peak is observed at 661 cm^{-1} as it is associated with the Sn-O stretching mode and Sn-O-Sn bond of the metal oxide. Fig 3.2(c) confirms the formation of SnO_2-GG nanocomposite. The broad peak at 3410 cm^{-1} is associated with the stretching vibrations of water molecules or –OH groups at the surface of metal oxide. The peak at 2930 and 1430 cm^{-1} corresponds to the –CH bending vibration. Peak obtained at 1080 cm^{-1} is attributed to the

stretching vibration of C-OH. Peak obtained at 611 cm^{-1} is corresponding to the asymmetric Sn-O-Sn stretching mode of metal oxide surface [46].

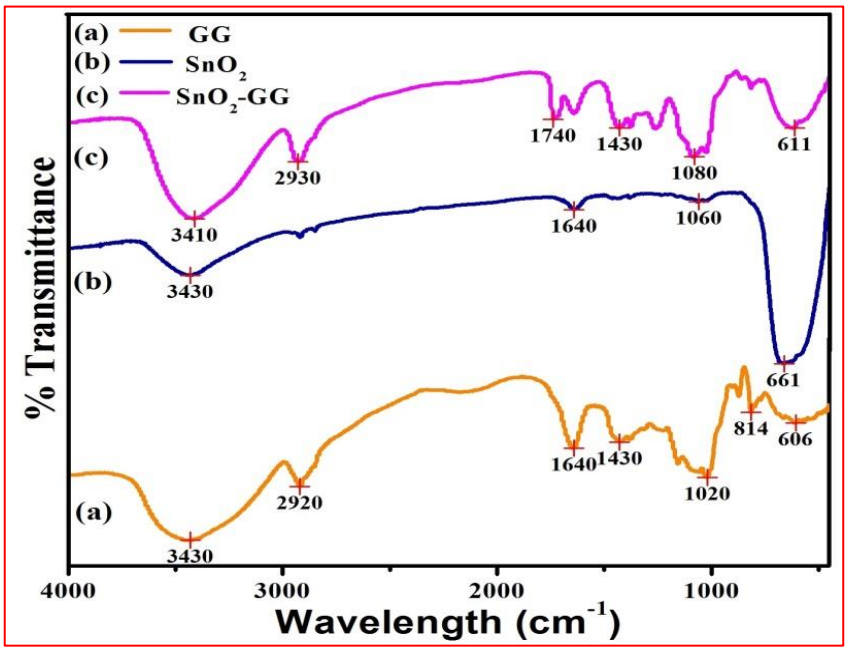

Figure 3.2: FT-IR transmission spectra of (a) GG, (b) SnO_2 nanoparticles and (c) SnO_2-GG nanocomposite

3.1.2 UV-Vis Spectroscopy Study

UV-Vis absorption spectroscopy studies were carried out by using Perkin Elmer, Lambda 950 to characterize the SnO_2 nanoparticles and SnO_2-GG nanocomposite. It also ascertains the presence of SnO_2 nanoparticles in the SnO_2-GG nanocomposite. Fig 3.2(b) shows UV-Vis absorption spectrum of the SnO_2 nanoparticles. The figure shows high absorption coefficient in the UV region, whereas it's low in the visible region. An absorption band is seen at 290 nm. Another absorption band seen at 365 nm is due to band to acceptor transition (band gap of ~3.3 eV) [47]. Fig 3.3(c) shows UV-Vis absorption spectrum of the SnO_2-GG nanocomposite. The absorption band is seen at 286 nm which confirms the presence of SnO_2 nanoparticles in GG nanocomposite.

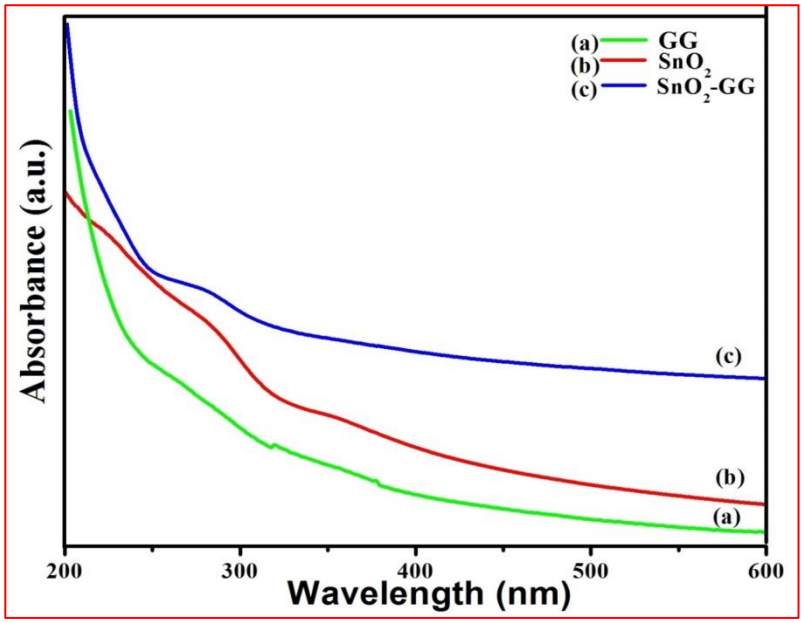

Figure3.3: UV-Vis absorption spectrum for (a) GG, (b) SnO_2 nanoparticles and (c) SnO_2-GG nanocomposite

3.1.3 Photoluminescence (PL) Spectroscopy Study

Fig.3.4 shows the emission spectra of (a) GG (b) SnO_2 nanoparticles and (c) SnO_2-GG nanocomposite. GG particles were excited at a wavelength of 280 nm whereas SnO_2 nanoparticles and SnO_2-GG nanocomposite, both exhibit emissions at 400 nm excitation. The optical properties of a semiconductor are related to both intrinsic and extrinsic effects. PL is a suitable technique to determine the crystalline quality and the presence of impurities in the materials as well as exciton fine structures. The emission maximum of 463 nm is obtained for SnO_2 nanoparticles; this is attributed to the contribution of oxygen vacancies and defect in the SnO_2 nanoparticles [48]. Since the energy of excitation and emission both are lower than the band gap of SnO_2 (E_g=3.56eV), therefore emission seems not due to the direct recombination of a conduction electron in the 4p band of Sn and a hole in the 2p valence band of O. GG PL peak was obtained at 436. In case of the SnO_2-GG nanocomposite, the emission spectrum showed a blue shift from the SnO_2 nanoparticle PL spectrum, and the emission maximum of 437 nm is obtained.

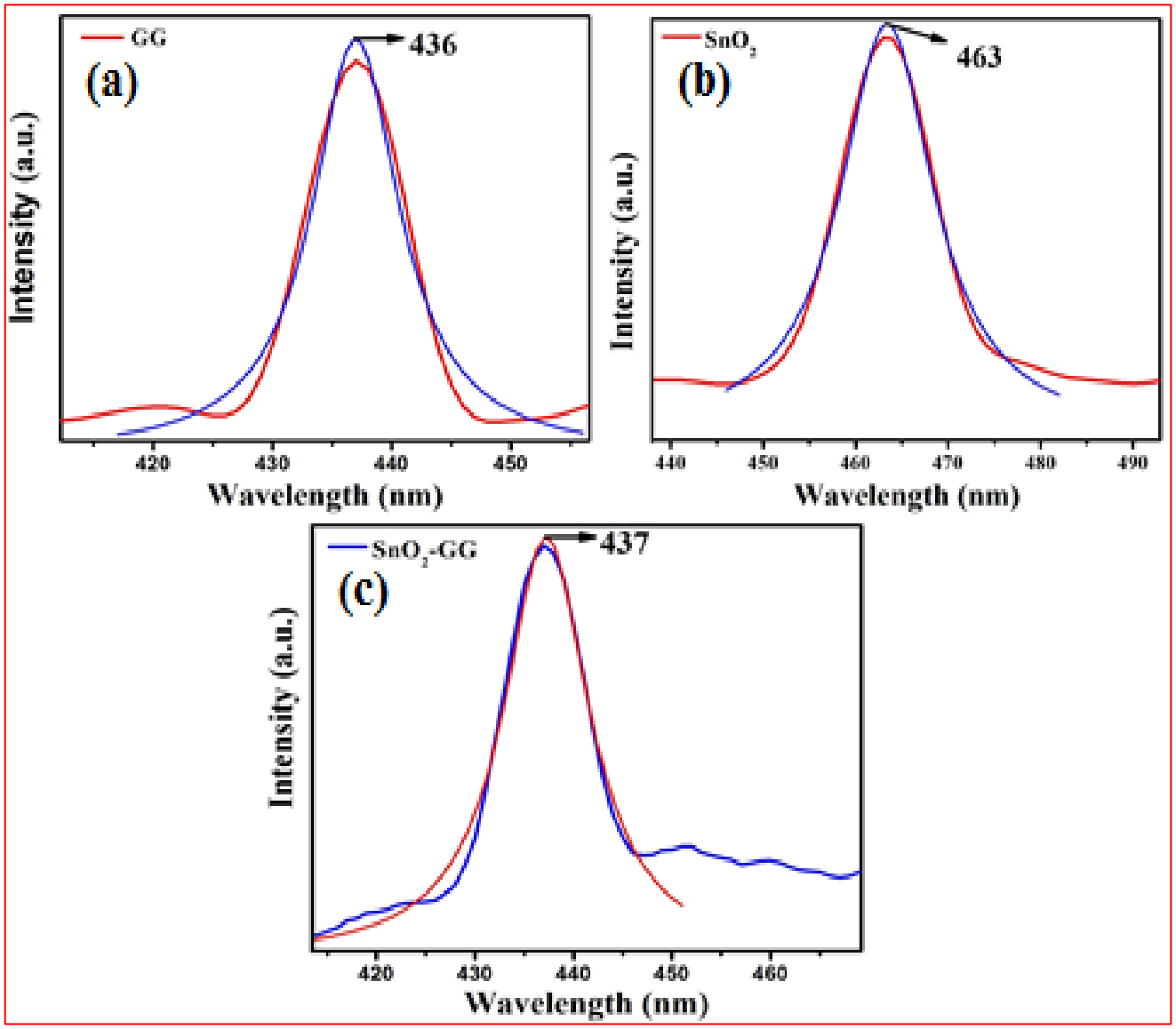

Figure 3.4: Photoluminescence emission spectra of (a) GG, (b) SnO_2 nanoparticles and (c) SnO_2-GG nanocomposite

3.2 Morphology analysis

3.2.1. AFM analysis

AFM evaluation was performed by using XE-100, Park System digital instrument by non-contact mode. AFM studies were carried out to investigate the surface properties for GG/ITO film, SnO_2/ITO film and SnO_2-GG/ITO nanocomposite film electrode in air environment. Fig 3.5(a) and (b) depicts the 2D and 3D atomic force microscopy images of for GG/ITO film, (c) and (d) for SnO_2/ITO film and (e) and (f) for SnO_2-GG/ITO nanocomposite film electrode, where from 3D view, the uniform height distribution throughout the surface is seen.

The morphology of the SnO_2/ITO electrode exhibit uniformly distributed SnO_2 nanoparticles on the surface of ITO; with root mean square roughness (R_q) = 1.039 nm, average roughness (R_a) = 0 .883 nm, maximum profile peak height = 9.123 nm. It can be seen that all nanoparticles on ITO surface are uniformly distributed with spherical shape.

The 3D surface morphology of GG/ITO film showed homogeneous and porous structural elements. The 2D and 3D morphology of SnO_2-GG/ITO nanocomposite film shows that nanoparticles get incorporated in GG layer with root mean square roughness (R_q) = 9.892 nm, average roughness (R_a) = 7.341 nm, maximum profile peak height = 27.702 nm. We obtained a rougher nanocomposite film as compared to SnO_2 nanoparticles with very well incorporated SnO_2 nanoparticles in GG biopolymer.

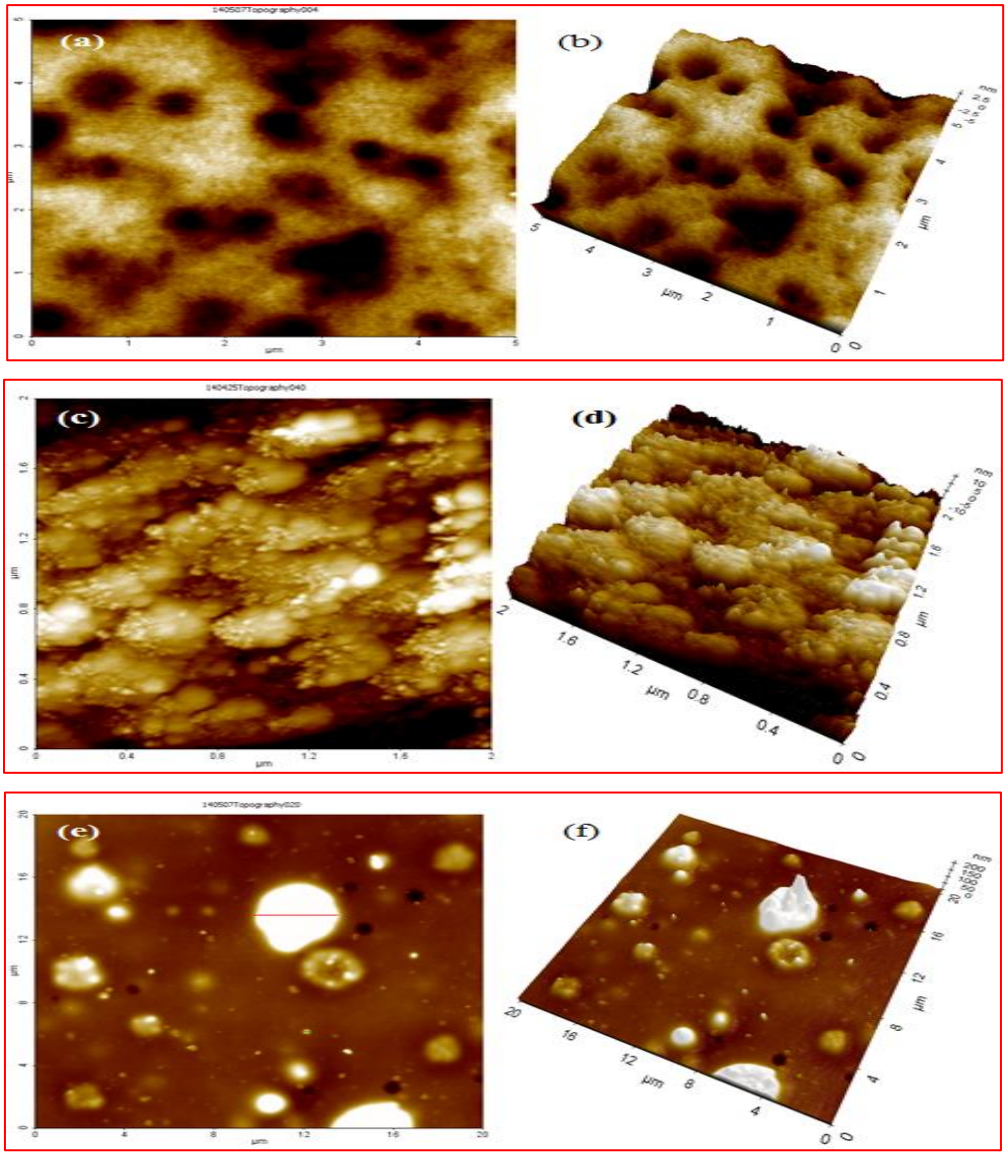

Figure 3.5: AFM analysis of (a) GG in 2D, (b) 3D, (c) SnO_2 nanoparticles in 2D, (d) 3D, (e) SnO_2-GG nanocomposite in 2D and (f) 3D

3.2.2. SEM analysis

The morphology of the SnO_2 nanoparticles and SnO_2-GG nanocomposite was investigated with the Scanning Electron Microscope. Fig 3.6(c) and (d) shows the agglomerated SnO_2 nanoparticles at 4 and 3 µ respectively. It shows the nearly spherical, uniformly distributed and highly crystalline nature of the nanoparticles. Fig 3.6(a) shows the SEM micrograph of GG powder taken at 200 µ. Fig 3.6(b) shows the SEM taken at 10 µ of GG film prepared by drop

casting method. GG particles appear to have coarse structure and irregularly shaped particles. SEM shows the amorphous nature of GG. Fig 3.6(e) and (f) shows the SEM micrograph of SnO_2-GG nanocomposite taken at 5 and 2 µ respectively. It clearly shows a change in appearance of SnO_2 nanoparticles due to the formation of nanocomposite with GG. Highly agglomerated particles with very small size and nearly spherical morphology can be seen easily in the nanocomposite.

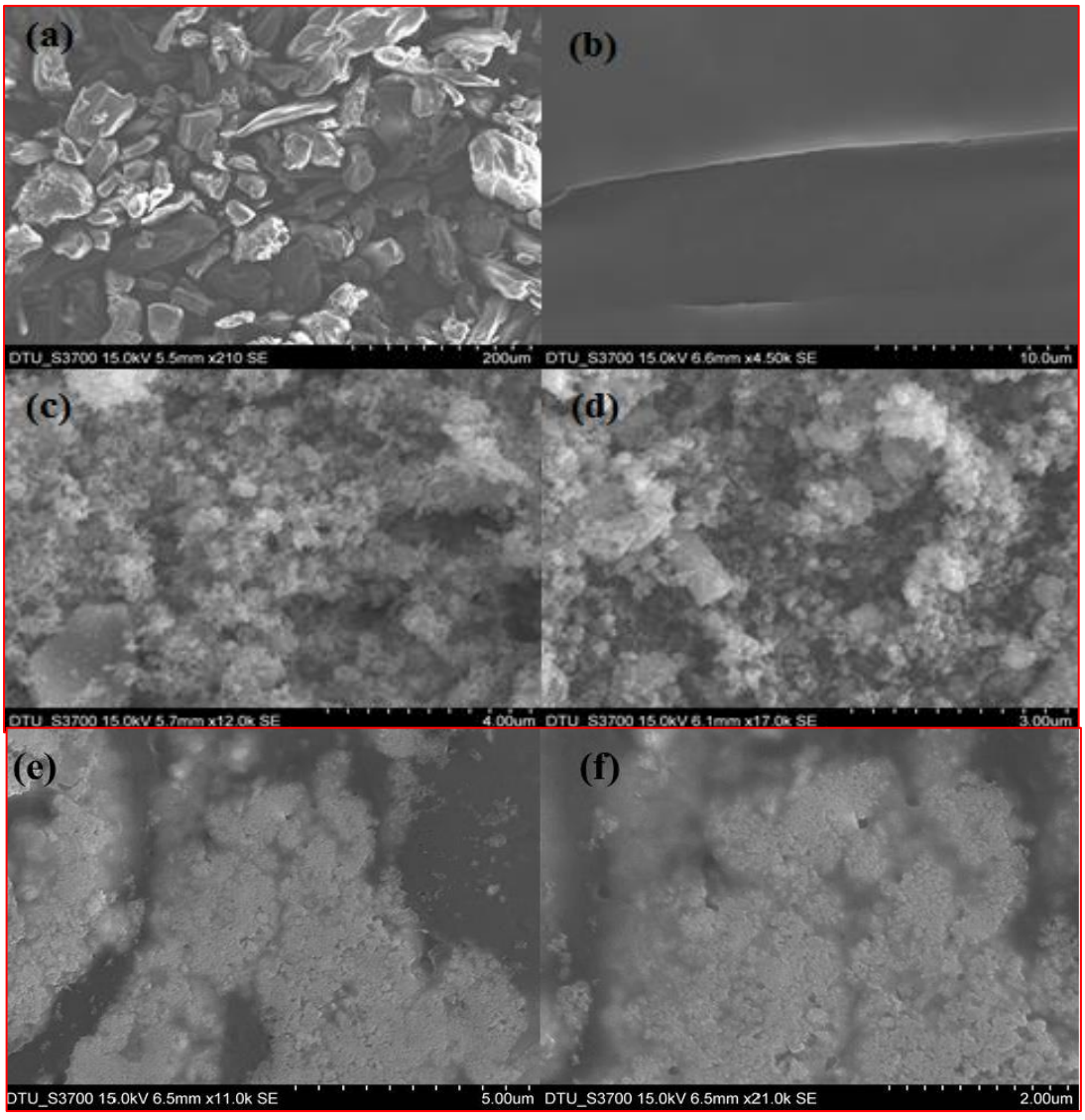

Figure 3.6: SEM micrograph of (a) GG powder, (b) GG film, (c) SnO_2 nanoparticles at 4 µ, (d) at 3 µ, (e) SnO_2-GG nanocomposite at 5 µ and (f) 2 µ

3.2.3. EDX analysis

The chemical composition of SnO_2 nanoparticles prepared at the optimized conditions was extracted from the energy dispersive X-ray spectrum (EDX) which is shown in Fig 3.7(b). The EDS analysis exhibited clear peaks of only Sn and O elements, whereas no additional peaks were detected, which means that the as-prepared prepared powder is exempted from impurities that arise from the starting precursors like silicon and carbon. The atomic percentages of Sn and O elements present in the as-prepared powder are 83.47 and 16.53 atom %, respectively.

The EDX analysis of GG clearly indicates the 83.69 and 16.31 atom % of C and O in guar gum. On preparation of the SnO_2-GG nanocomposite, the EDX analysis confirms the presence of only Sn, O and C elements. It means the nanocomposite is free from any form of impurity.

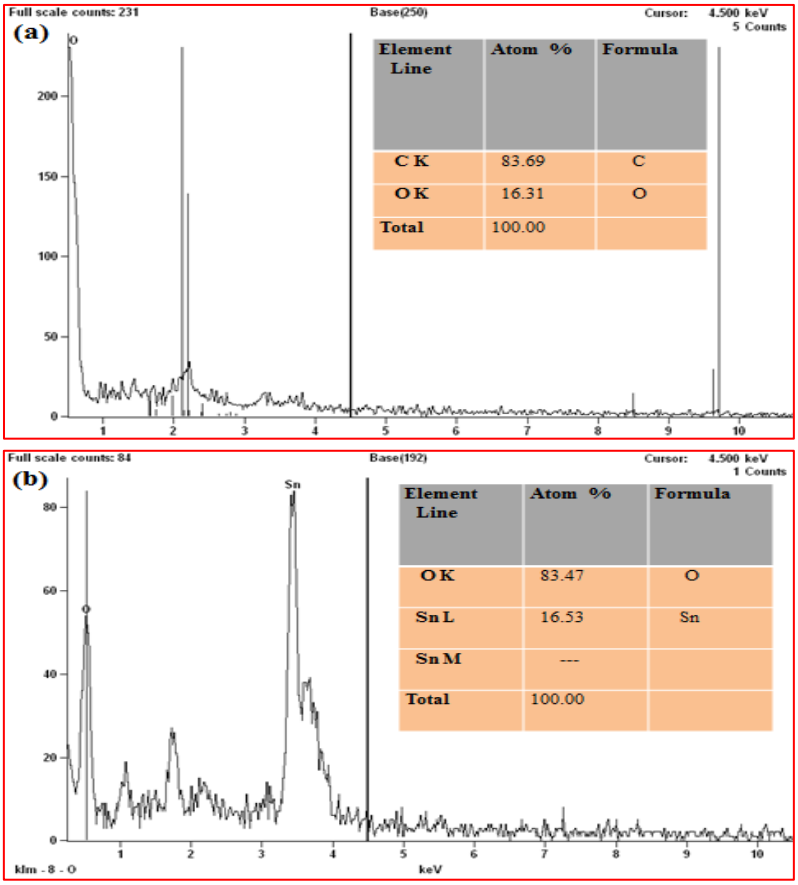

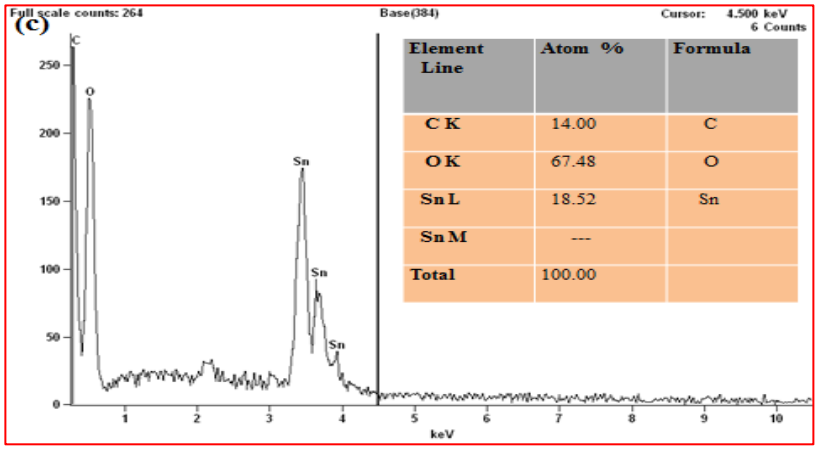

Figure 3.7: EDX analysis of (a) GG, (b) SnO_2 nanoparticles and (c) SnO_2-GG nanocomposite

3.2.4. TEM analysis

Fig 3.8(a) and (b) shows the TEM micrograph of as-prepared SnO_2 powder at 20 nm. It is clear from the figure that the SnO_2 nanoparticles are highly crystalline in nature and uniformly distributed. It consists of a mixture of oval and nearly spherical nanocrystals of SnO_2 with an average particle size of ~11 nm which is in good agreement with that estimated by the X-ray diffraction pattern.

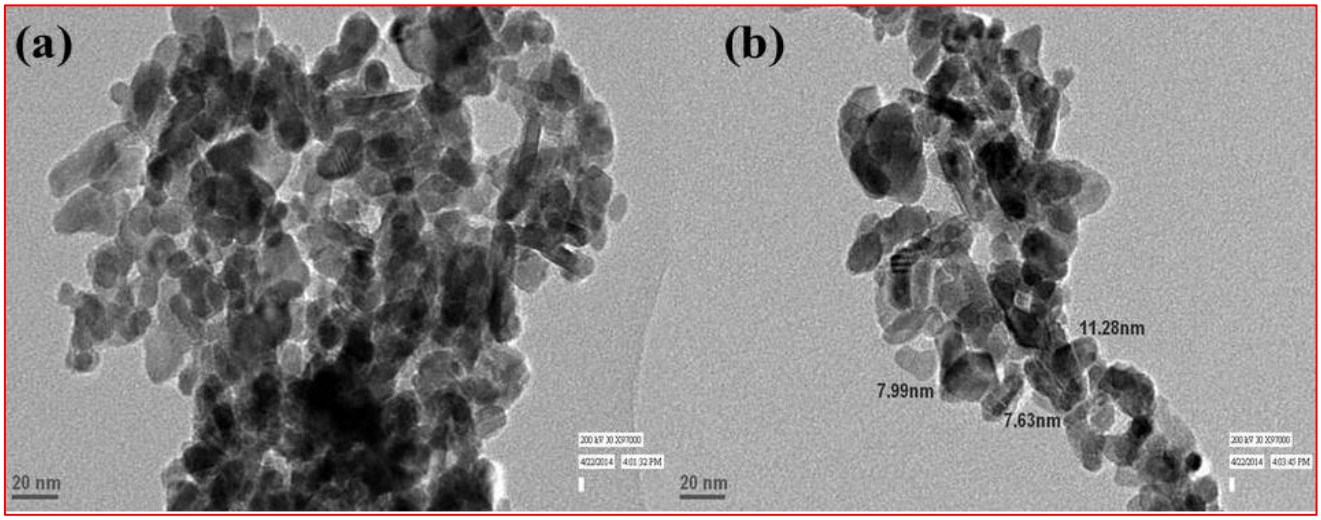

Figure 3.8: (a) and (b) TEM micrographs of SnO_2 nanoparticles at 20 nm

3.3 Electrochemical studies

3.3.1. CV and DPV studies

The electrochemical behavior of SnO_2 on the modified electrodes was investigated by cyclic voltammetry. Fig 3.9 shows the cyclic voltammograms of the different electrodes in PBS (5 mM, pH 7.0, 0.9% NaCl) containing $[Fe(CN)_6]^{3-/4-}$ (5 mM) at a scan rate of 50 mV/s. The CV of the bare ITO (Fig 3.9(a)) exhibits electrochemical characteristics with a couple of redox peaks for the $[Fe(CN)_6]^{3-/4-}$ mediator, and shows an oxidation peak current (I_{pa}) of 0.27 mA. After its modification with GG, the I_{pa} value is enhanced to 0.30 mA (Fig 3.9(b)). The peak current of the SnO_2/ITO electrode (Fig 3.9(c)) (I_{pa}) 0.47 mA is higher than those of GG/ITO and bare ITO, which can be ascribed to the excellent conductivity and large surface area of the SnO_2 nanoparticles. After the insertion of SnO_2 nanoparticles in the GG matrix of the SnO_2-GG/ITO electrode, the peak current increased up to 0.51 mA (Fig 3.9(d)), indicating the good conductivity of the SnO_2 nanoparticles. The oxidation peak potential (E_{pa}) and reduction peak potential (E_{pc}) are located at 0.39 and 0.041 V, respectively [49].

The results of differential pulse voltammetric (DPV) studies reveal similar behavior of the redox potential towards the SnO_2-GG/ITO electrode (Fig 3.10).

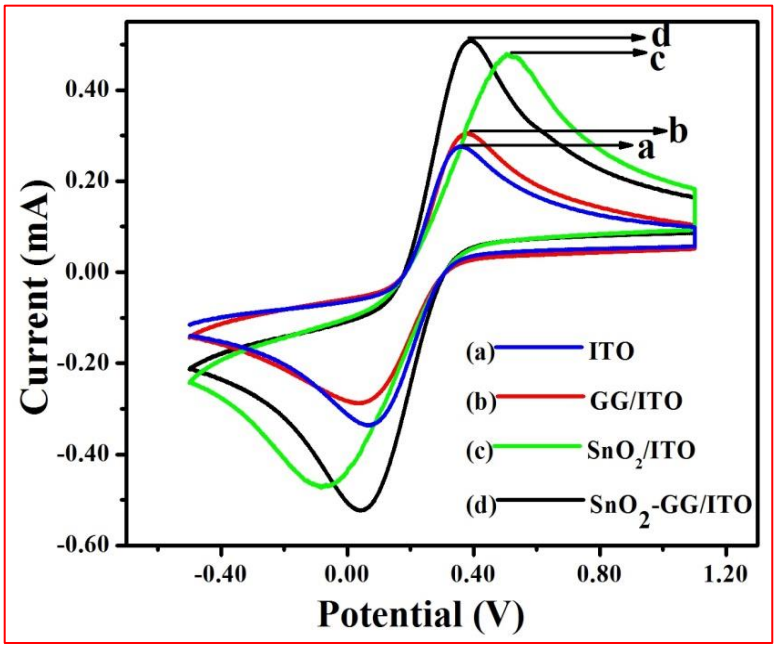

Figure 3.9: Cyclic voltammogram of (a) bare ITO electrode, (b) GG/ITO electrode, (c) SnO_2/ITO electrode and (d) SnO_2-GG/ITO electrode

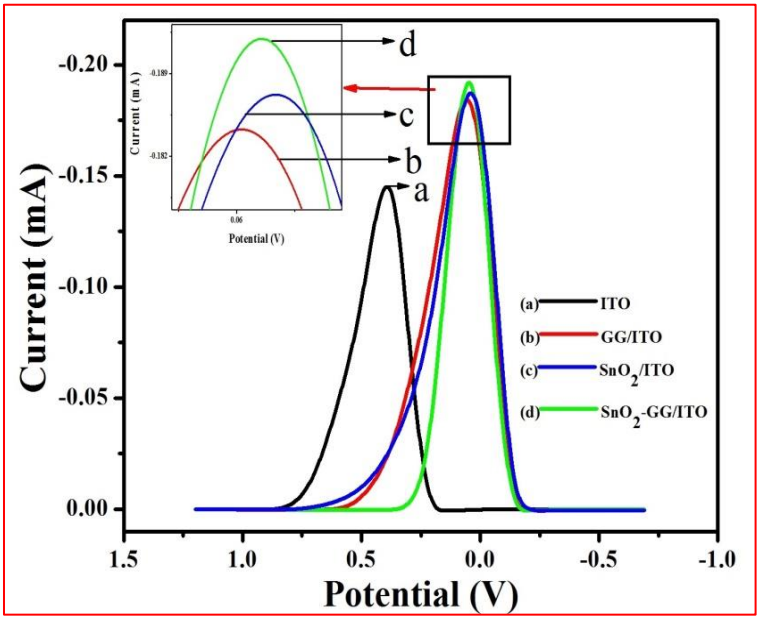

Figure 3.10: DPV of (a) bare ITO electrode, (b) GG/ITO electrode, (c) SnO_2/ITO electrode, and (d) SnO_2-GG/ITO electrode

3.3.2. Scan rate studies

To investigate the interfacial kinetics of the SnO_2-GG/ITO electrode surface, CV studies have been conducted as a function of scan rate varying from 10 to 100 mV s^{-1} (Fig 3.11). It can be seen that magnitudes of both anodic (I_{pa}) and cathodic (I_{pc}) peak currents increase linearly with square root of scan rate ($\nu^{1/2}$) (Fig 3.11). With increasing scan rate the oxidation peak shifts towards more positive potential and similarly reduction peak shifts towards more negative potential, indicating that the redox process is quasi-reversible.

The value of electron transfer co-efficient (α), for n number of electrons, has been calculated from two straight lines with a slope equal to $2.3RT/(1 - \alpha)nF$ for the anodic peak and $-2.3RT/\alpha nF$ for the cathodic peak, using Laviron's equations [50]. The electron transfer co-efficient (α) for the SnO_2-GG/ITO electrode has been found to be 0.913966 V for anodic peak and 0.0790355 V for cathodic peak.

The change in value of the charge transfer rate constant (K_s) of the electrode due to surface modification has been calculated
by following eq 3.2.

$$K_s = mnF\,\nu/RT \qquad \text{……….…………………………..} \ (3.2)$$

where m is the peak-to-peak separation (V), F is the Faraday constant (96 485 C mol^{-1}), ν is the scan rate (30 mV s^{-1}), n is the number of transferred electrons (1), R is the gas constant (8.314 J mol^{-1} K^{-1}) and T is the room temperature (25 °C).
The K_s value of the SnO_2/ITO electrode and the SnO_2-GG/ITO electrode has been found to be 1.312313 and 0.68682 s^{-1} respectively. The increased K_s value at the surface of the SnO_2/ITO electrode clearly indicates that both the electronic structure and surface physicochemistry of the SnO_2 nanoparticles contribute to increased electron transfer arising from high catalytic behavior of SnO_2 nanoparticles.

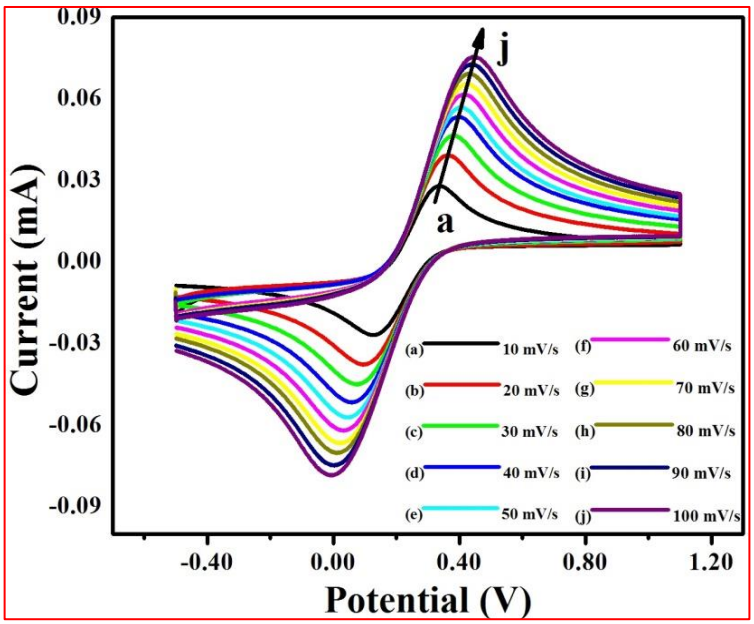

Figure 3.11: Cyclic Voltammogram of SnO_2-GG/ITO electrode with increasing scan rate from 10 mV/s to 100 mV/s

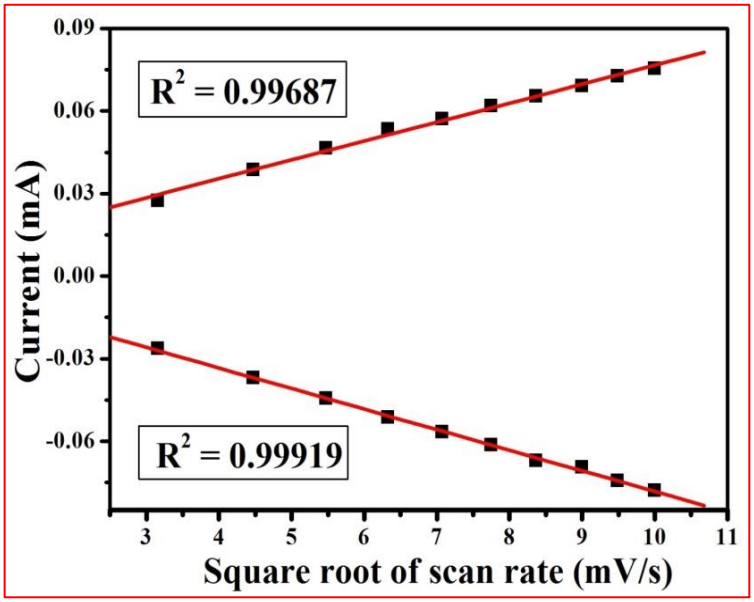

Figure 3.12: Magnitude of current versus potential difference as a function of square root of scan rate (10-100 mV/s)

The anodic (E_{pa}) and cathodic (E_{pc}) peak potentials and potential peak shift ($\Delta E_p = E_{pa} - E_{pc}$) exhibit a linear relationship (see Fig 3.13) with scan rate. These results reveal that the chemical reaction at the electrode is a diffusion controlled process. The diffusion co-efficient value (D) for free diffusion of $[Fe(CN)_6]^{3-/4-}$ from electrolyte solution to the corresponding electrode surface has been calculated using the Randles–Sevcik eq 3.3 [50].

$$I_p = (2.69 \times 10^5)\, n^{3/2} A D^{1/2} C\, v^{1/2} \qquad \text{(3.3)}$$

where I_p is the peak current of the corresponding electrode (I_{pa} anodic and I_{pc} cathodic), n is the number of electrons involved or electron stoichiometry (1), A is the surface area of the electrode (0.25 cm^2), D is the diffusion co-efficient, C is the surface concentration in mol (5 mM) and ν is the scan rate (50 mV/s). The value of D for the for SnO_2-GG/ITO electrode is obtained as 4.3121×10^3 $cm^2 s^{-1}$.

The surface concentration of the electrodes has been estimated using the Brown−Anson model [51] by following eq 3.4.

$$I_p = n^2 F^2 I^* A V / 4RT \qquad \text{(3.4)}$$

where n is the number of electrons transferred (1), F is the Faraday constant (96485 C/mol), I^* is the surface concentration of the corresponding electrode (mol cm^{-2}), A is the surface area of the electrode (0.25 cm^2), V is the scan rate (30 mV/s), R is the gas constant (8.314 J mol^{-1} K^{-1}), and T is the room temperature (25 °C). The surface concentration of SnO_2-GG/ITO (4.32603×10^{-8} mol cm^{-2}) is higher than that of SnO_2/ITO (4.08095×10^{-8} mol cm^{-2}).

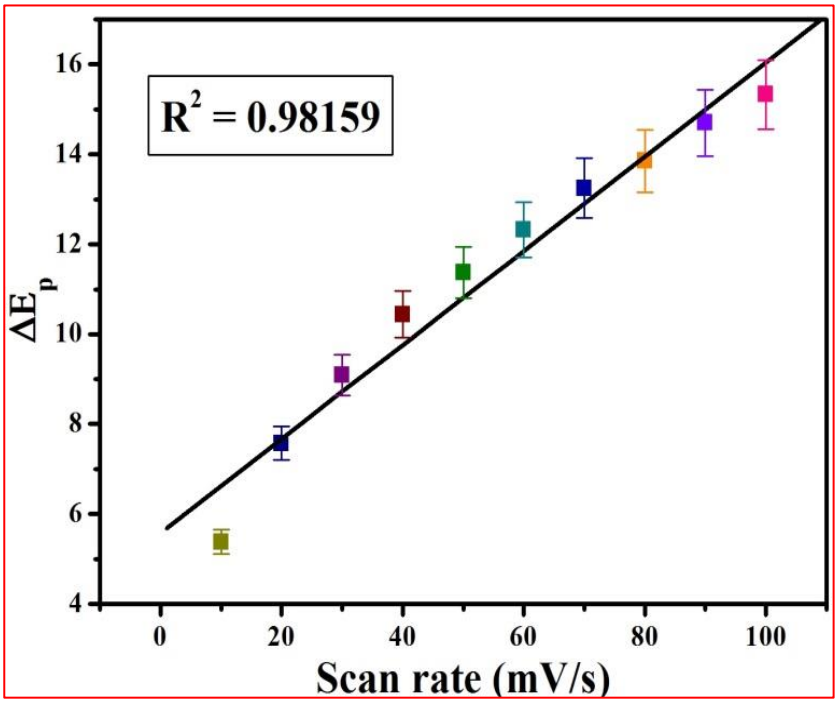

Figure 3.13: Potential peak shift v/s scan rate

3.3.3. Optimization of pH

The effect of solution pH (5.7 to 8.0) on the electrochemical behavior of the SnO_2-GG/ITO electrode is measured by the CV technique in PBS (5 mM, 0.9% NaCl) containing $Fe(CN)_6]^{3-/4-}$ (5 mM) at a 50 mV s^{-1} scan rate(Fig 3.14). It can be seen that the oxidation peak current increases from 5.7 to 7.0 and the highest magnitude of current is obtained at 7.0. The E_{pa} value decreases from 5.7 to 6.4 and then increases from 6.4 to 7.0, again decreasing on increasing pH to 8.0. The limited electron transport between the medium and the electrode may lead to a decrease in the electrochemical signal at higher pH (8.0). These changes in the peak current may arise due to a decrease in concentration of the positively charged moieties (Sn^{2+}) present at the matrix as the pH of PBS approaches its isoelectric point (IEP); this could result in decreased interaction between redox ions $[Fe(CN)_6]^{3-/4-}$ and the SnO_2/ITO surface. Thus pH 7 is selected as the optimum pH for further experiments.

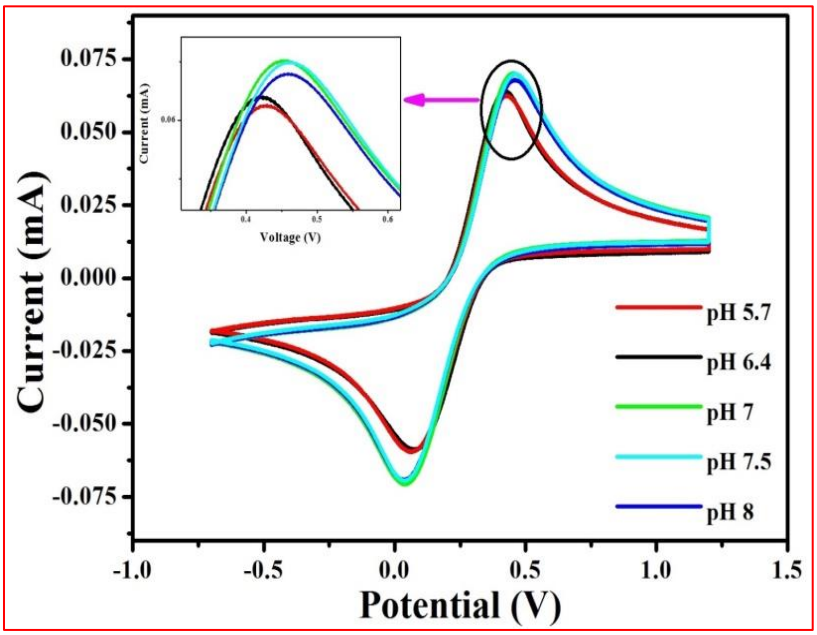

Figure 3.14: CV studies of the SnO_2-GG/ITO electrode as a function of pH (ranging from 5.7 to 8.0 in phosphate buffer containing $[Fe(CN)_6]^{3-/4-}$

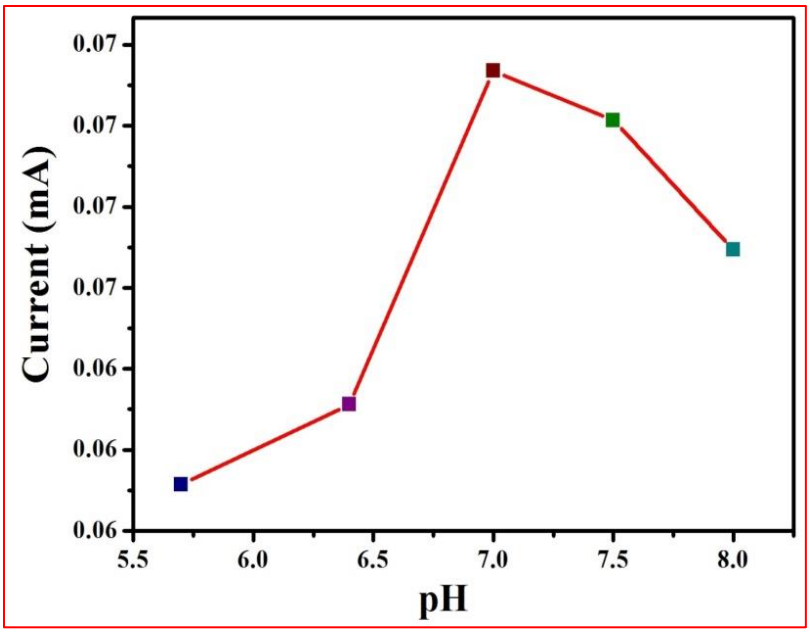

Figure 3.15: Change in current response as a function of the SnO_2-GG/ITO electrode pH

3.3.4. Electro-oxidation studies of hydrazine

The overall reaction for the oxidation of hydrazine can be written as follows:

$$N_2H_4 + 4OH^- \rightarrow N_2 + 4H_2O + 4\,e^- \qquad \text{……..…….. (3.5)}$$

The effect of hydrazine concentration on the CV response of SnO_2-GG/ITO electrode has been investigated in 5 mM phosphate buffer (PBS, pH = 7.0, 0.9% NaCl) containing $[Fe(CN)_6]^{3-/4-}$ at a scan rate of 50 mV/s. Fig 3.16 shows CV of the SnO_2-GG/ITO electrode as a function of hydrazine concentration varying from 2-22 mM. With increasing hydrazine concentration in the solution, the anodic peak current increases. It is observed that the oxidation current of hydrazine first rises and then reaches a maximum value at ~ 0.52 V. This catalytic peak current has a linear relationship with the concentration of hydrazine in the range of 2-22 mM. Linear calibration is obtained, with a coefficient of 0.9892, demonstrating the good relationship between oxidation current and concentration. The limit of detection (LOD) has been estimated to be 2.769 mM, linearity is 2-22 mM and sensitivity is 5.72 μMcm^{-2}. From these results, it can be concluded that electro-oxidation of hydrazine at this electrode can be used for quantitative determination of hydrazine in given samples and it thus has a potential application as electro-oxidation device.

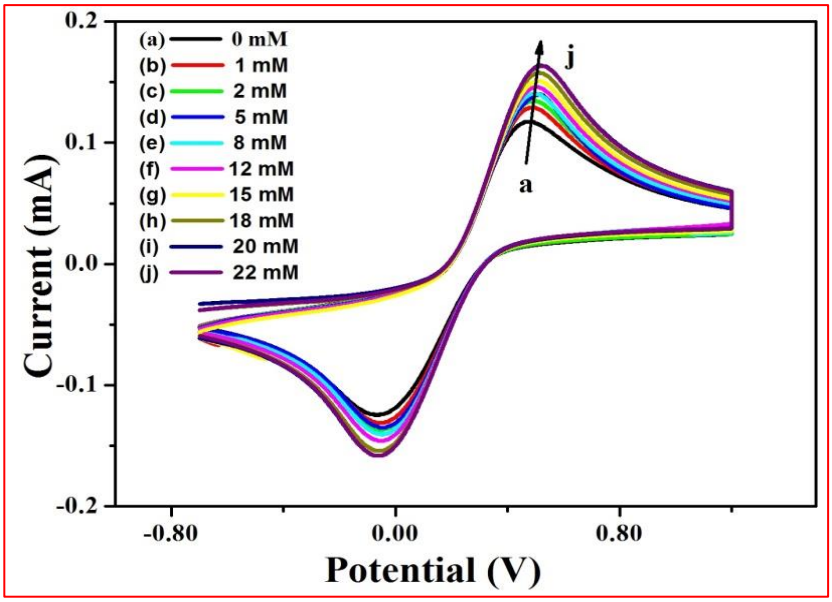

Figure 3.16: Electrochemical response of the SnO_2-GG/ITO electrode with respect to hydrazine concentration (2-22 mM) in PBS (5 mM, 7.0 pH, 0.9% NaCl) containing $[Fe(CN)_6]^{3-/4-}$ at a scan rate of 50 mV/s

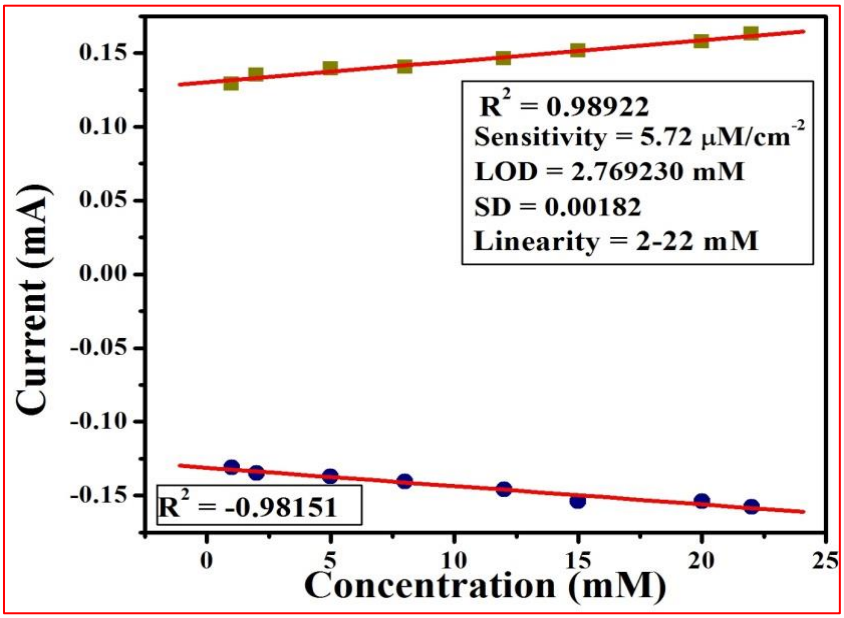

Figure 3.17: Calibration curve of the SnO_2-GG/ITO electrode and the variation in current as a function of hydrazine concentration (2-22 mM) in PBS (5 mM, 7.0 pH, 0.9% NaCl) containing $[Fe(CN)_6]^{3-/4-}$ at a scan rate of 50 mV/s

3.3.5. Response time studies

For the determination of response time (Fig 3.18) of SnO_2-GG/ITO nanocomposite electrode, we have measured electrochemical current response from 2 to 40 s. The magnitude of current increases initially and achieves maximum value at 35 s. After 35 s the value of current starts decreasing, indicating that 35 s is the response time for SnO_2-GG/ITO nanocomposite electrode.

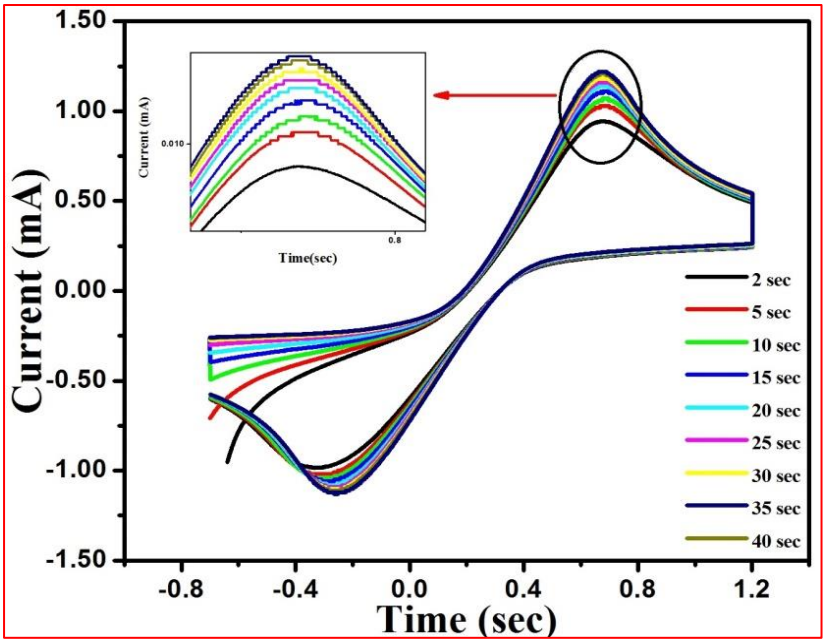

Figure 3.18: CV study of electrochemical response time of SnO_2-GG/ITO nanocomposite electrode incubated for a time period of 2-40 s

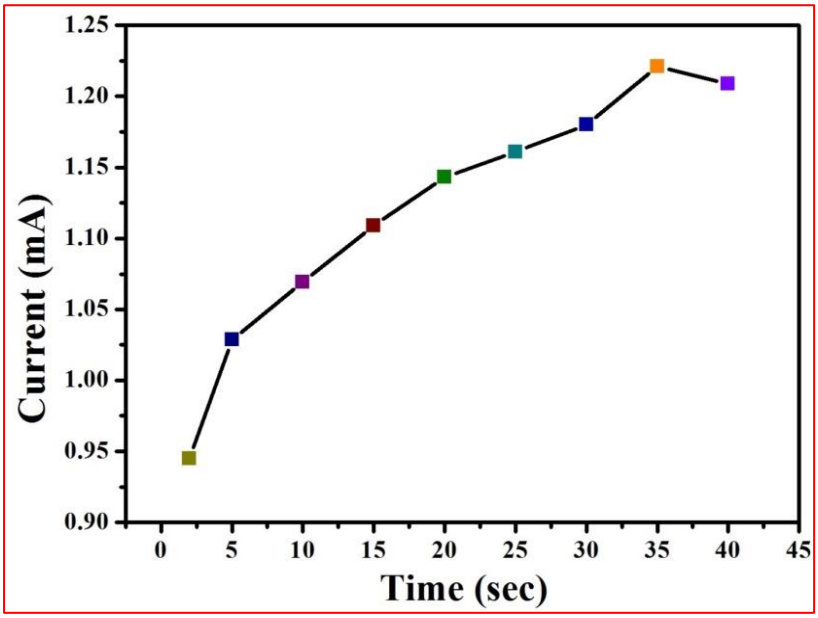

Figure 3.19: Electrochemical response time for incubation of SnO_2-GG/ITO nanocomposite electrode from 2 to 40 s

3.4 Antibacterial activity assay

The antibacterial activity of the SnO_2 nanoparticles, GG and SnO_2-GG nanocomposite was tested against *Bacillus cereus* and *Pseudomonas aeruginosa* .i.e. Gram positive and Gram negative bacteria respectively. A concentration dependent study was carried out for the SnO_2-GG nanocomposite against *B. cereus* and *P. aeruginosa* and it showed that even at low concentration of SnO_2-GG, nanocomposites shows better results as compared to high concentration. Nanostructured SnO_2 taken at 1 mg/ml concentration gave an inhibition zone of 1 mm against *B. cereus* and 2.5 mm zone against *P. aeruginosa*. An inhibition zone of 0.5 mm was observed with both the strains at 0.25 mg/ml concentration of SnO_2-GG nanocomposites. SnO_2-GG nanocomposite showed an inhibition zone of 3 mm against *P. aeruginosa*. The higher deactivation efficiency towards the Gram –ve bacteria as compared to the Gram +ve bacteria has been reported earlier, hence the results agree well to that. The difference in result can be attributed to the difference in cell wall structure of the Gram +ve and Gram –ve bacteria. Gram positive and Gram negative bacteria have similar internal, but very different structures [51]. A Gram positive peptidoglycan layer that contains teichoic and lipoteichoic acids. A Gram negative bacterium has a thin peptidoglycan layer and an outer membrane that contains lipopolysaccharide, phospholipids, and proteins.

Bacterial Strain	**Bacterial Strain Name**	**Inhibition zone of various samples against bacterial growth (mm)**			
		SnO_2 (1mg/ml)	**GG (1mg/ml)**	**SnO_2-GG (1mg/ml)**	**SnO_2-GG (0.25mg/ml)**
Gram +ve	*Bacillus cereus*	1	-	-	0.5
Gram -ve	*Pseudomonas aeruginosa*	2.5	1	3	0.5

Table 3.1: Concentration dependent antibacterial activity given by various nanoparticles and nanocomposite

GG alone did not give any considerable antibacterial activity against the Gram positive strain, while an inhibition zone of 1 mm was obtained for *P. aeruginosa*.

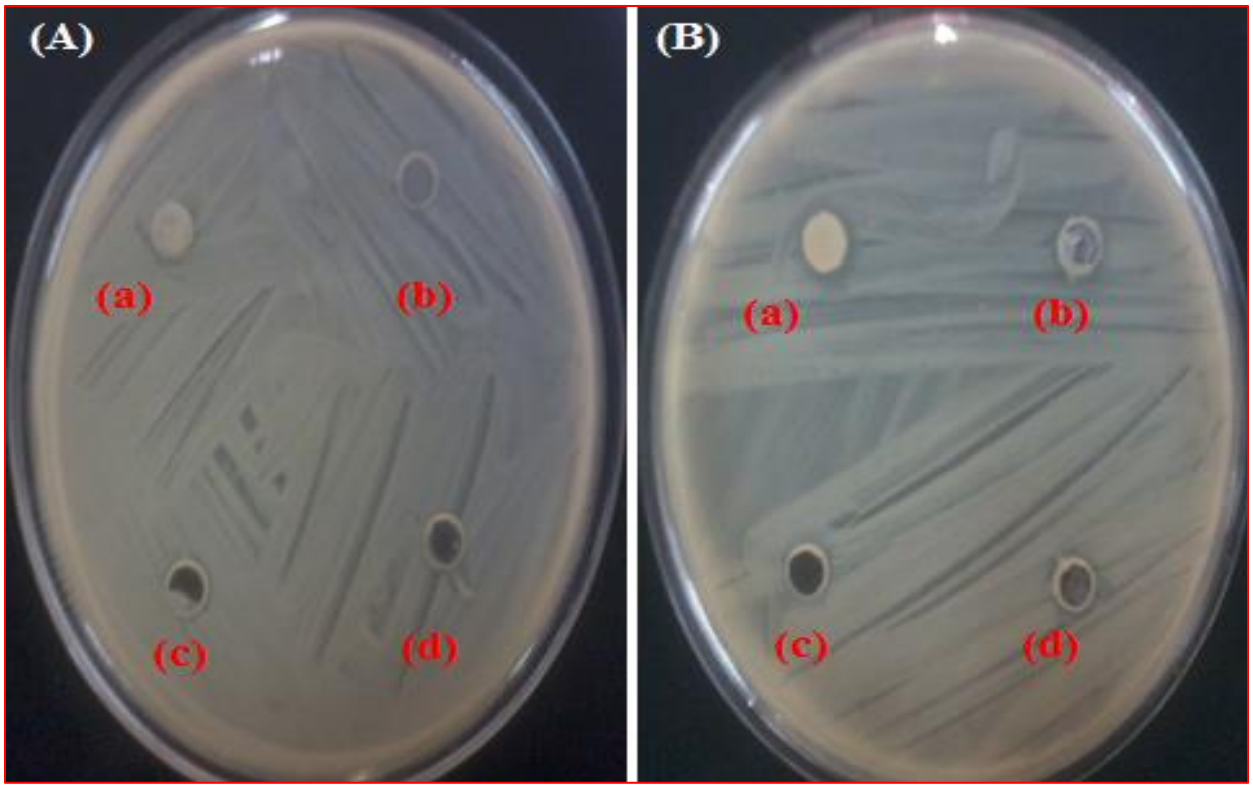

Figure 3.20: Antibacterial activity against (A) *B.cereus*, and (B) *P. aeruginosa* showing various samples (a) SnO_2, (b) GG, (c) SnO_2-GG at 1 mg/ml and (d) SnO_2-GG at 0.25 mg/ml

4. Conclusion and future prospects

4.1. Conclusion

We have fabricated an amperometric non enzymatic sensor by binding the SnO_2 nanoparticles (10.6 nm) with the GG matrix. The SnO_2 nanoparticles were synthesized by sol-gel method. SnO_2 nanoparticles were dispersed in GG solution ultrasonically and were casted onto ITO surface by drop casting method. The SnO_2-GG/ITO electrode showed rapid response (35 s), high sensitivity 5.72 μMcm^{-2}, linearity (2-22 mM), standard deviation (0.00182), low detection limit (2.769 mM), good reproducibility and long term stability. The wide detection range and high sensitivity may be assigned to the amplification of the magnitude of current response since the presence of SnO_2 nanoparticles in guar gum matrix and its good biocompatibility improves the electron transfer between analyte (hydrazine) and SnO_2-GG/ITO electrode surface. The results clearly suggest that SnO_2-GG nanocomposite electrode provides an attractive matrix for impregnation of metal-oxide nanoparticles and an improved non-enzymatic sensor for the electrochemical studies.

4.2 Future prospects

Electroanalysis is a complementary technique to other analytical techniques. In this field, many of the existing analytical techniques cannot be applied as they require complex and large equipment, and so, electrochemical monitoring can bring many advantages. In the laboratory, the detection limits possible in electroanalysis make it a strong competitor for many other analytical techniques when alternatives exist. The advantage of distinguishing oxidation states is highly important. The electrochemical approach can give a rapid answer, without digestion, as to the labile fraction of a given element in a particular oxidation state, and the experiment can be performed on-site in the field. Hence recent developments are focusing on development of sensors to detect even nanometer range of materials in the environment.

Hydrazine and its derivatives have found a wide range of applications, including as antioxidants, pharmaceutical intermediates, pesticides, plant-growth regulators, blowing agents, corrosion inhibitors, dyes and in photography. Furthermore, hydrazine is a high energy fuel

molecule and reducing agent as well and can be used as the fuel in explosives and rocket propulsion systems. Direct hydrazine (N_2H_4)-air fuel cells are highly attractive because of their superior theoretical standard equilibrium potential and high power density. It is mainly used as a foaming agent, but uses as a precursor to polymerization catalysts and pharmaceuticals. Hydrazine hydrate and its derivatives react with benzothiazole derivatives and synthesized newly compound wear evaluated for antibacterial activity. Hydrazine is extensively used in many industries like power plant to reduce corrosion of metal pipes and fittings.

Nevertheless, hydrazine is toxic and probably even potentially carcinogenic. In order to better utilize hydrazine as a fuel and resolve these environmental issues, the development of a catalyst that can oxidize at a high rate is required. However, a major barrier to the wide application of direct hydrazine (N_2H_4)-air fuel cells is the expensiveness of the noble metal catalysts that are generally required. To overcome this problem, research has been focused on developing various types of catalysts for the electro-oxidation of hydrazine.

However, very limited research has been done towards the sensing and electro-oxidation of hydrazine. This project work has tried to work towards this field using metal oxide-biopolymer nanocomposite. Nanoparticles have suitable physical and chemical properties for the development of electrochemical sensors and biosensors. Sensors with improved stability can be prepared using nanoparticles as substrate for biomolecules immobilization, while electrochemical sensors with improved sensitivity and selectivity can be developed making use of the catalytic properties of nanoparticles.

The emergence of nanotechnology is opening new horizons for electrochemical sensors. Recent years have witnessed the development of a variety of nanomaterials based devices exhibiting novel functions. The use of nanomaterials in such sensing devices has taken off rapidly and will surely continue to expand. Nanoparticles, nanowires and nanotubes have already made a major impact on the field of electrochemical sensors and the unique properties of nanomaterials suggest that future interdisciplinary research could lead to a new generation of electrochemical biosensors. A wide range of newly introduced nanomaterials is expected to expand the field of nanomaterials based sensors. Such nanomaterials based electrochemical

devices are expected to have a major impact upon clinical diagnostics, environmental monitoring, security surveillance and food safety.

REFERENCES

1. S. Logothetidis (ed.), NanoScience and Technology, DOI 10.1007/978-3-642-22227-61.
2. K.D. Sattler, *Handbook of Nanophysics, Principles and Methods* (CRC, New York, 2010).
3. B. Bhushan, *Handbook of Nanotechnology* (Springer, Berlin, 2004).
4. J.V. Barth, G. Costantini, K. Kern, Nature 437, 671–679 (2005).
5. L. Chou, Y. Cai, B. Zhang, J. Niu, S. Ji, S. Li, Appl. Catal. A: Gen. 238 (2003) 185.
6. P.T. Wierzchowski, L.W. Zatorski, Appl. Catal. B: Environ. 1352 (2003) 1.
7. A.J. Moulson, J.M. Herbert, Electroceramics, Chapman & Hall, New York, (1990).
8. Y. Shimizu, M. Egashira, MRS Bull. 24 (1999) 18.
9. M. Kojima, F. Takahashi, K. Kinoshita, T. Nishibe, Ichidate, Thin Solid Films 392 (2001) 349.
10. C.M. Lampert, Sol. Ener. Mater. 6 (1981) 1.
11. J.F. Wang, Y.J. Wang, W.B. Su, H.C. Chen, W. X . Wang, Mater. Sci. Eng. B 96 (2002) 8.
12. M.R.C. Santos, P.R. Bueno, E. Longo, J.A. Varela, J. Eur. Ceram. Soc. 21 (2001) 161.
13. T.E. Moustafid, H. Cachet, B. Tribollet, D. Festy, Electrochim. Acta 47 (2002) 1209.
14. M. Okuya, S. Kaneko, K. Hiroshima, I. Yaggi, K. Murakami, J. Eur. Ceram. Soc. 21 (2001) 2099
15. T.W. Kim, D.U. Lee, D.C. Choo, J.H. Kim, H.J. Kim, J.H. Jeong, M. Jung, J.H. Bahang, H.L. Park, Y.S. Yoon, J.Y. Kim, J. Phys. Chem. Solids 63 (2002) 881.
16. P.G. Harrison, M.J. Willet, Nature 1988, 332,337.
17. J.J.Zhu, Z.H.Lu, S.T.Aruna, D Aurbach, A. Gedanken, *Chem Mater*. 2000, 12, 2557.
18. S. Ferrere, A Zaban, B. A. Gregg, *J. Phys Chem.* 1997, 101, 4490.
19. N. A. Madzlan, S. S. Abbas, W. Rosemaria, W. Baharom, Materials Letters 91 2013, 31-34.
20. A. Ayeshamariam, C.Sanjeeviraja, and R. Perumal Samy, Journal on Photonics and Spintronics Vol2 No2 May 2013 ISSN 2324 -8572.
21. G. E Patil , D. D Kajale 2, V. B Gaikwad and G. H Jain, Patil et al. International Nano Letters 2012, 2:17.

22. C. L. O. Petkowicz, F. Reicher and K. Mazeau, *Carbohydr. Polym.* **37** (1998) 25-39.
23. G. A. Morris, T. R. Patel, D. R. Picout, S. B. Ross-Murphy, A. Ortega, J. G. de la Torre and S. E. Harding, *Carbohydr. Polymers* **72** (2008) 356-360.
24. P. J. H. Daas, H. A Schols and H. H. J. de Jongh, *Carbohydr. Res.* **329** (2000) 609-619.
25. L. Pitkänen, P.i Tuomainen, K. S. Mikkonen andM. Tenkanen, *Carbohydr. Polymers* **86** (2011) 1230-1235.
26. http://www.guargum.biz/guargum_chemical_structure.html.
27. http://www1.lsbu.ac.uk/water/hygua.html.
28. R. Gardner, Goodbye guar? *Int. Food Ingredients* **2** (2012) 40.
29. Z. Jingchang, F. Liye, W. Jia, G. Xuehua & C. Weiliang, Chinese Science Bulletin September 2006, Volume 51, Issue 17, pp 2050-2054.
30. A. I. Aparnev, A. A. Golubchuk, I. S. Chukanov, N. F. Uvarov, Glass Physics and Chemistry February 2012, Volume 38, Issue 1, pp 131-136.
31. V. S. Reddy Channu, Rudolf Holze, Ionics,May 2012, Volume 18, Issue 5, pp 495-500.
32. R. G. Auddy , Md F. Abdullah , S. Das , P. Roy , S. Datta, Arup Mukherjee, BioMed Research International 2013 Vol: 2013:DOI: 10.1155/2013/912458.
33. X. Shi, W. Wang, A. Wang, Journal of Polymer Research November 2011, Volume 18, Issue 6, pp 1705-1713.
34. T. Blanton, C. Barnes, J. Putrelo, A. Yeboah, S. Switalski, International Centre for Diffraction Data 2004, Advances in X-ray Analysis, Volume 47.
35. R. Sharma, D.P. Bisen, U. Shukla and B.G. Sharma, Recent Research in Science and Technology 2012, 4(8): 77-79 ISSN: 2076-5061.
36. Available from http://www.eserc.stony brook.edu/ Project Java/Bragg.
37. W. Kemp, Organic Spectroscopy‟, *The Macmillan Press Ltd*, 1991, Houndmills, Basingstoke, Hampshire.
38. J. J. Storf, A. D. Lucas, V. Garmella, Y. P. Bao and U. R. Muller, *Nat. Biotechol*., 22, 2004, 283.
39. http://www.learner.org/courses/physics/visual/visual.html?shortname=michelson.
40. X. M. Yang , Z. Z. Gu, Z. H. Lu and Y. Wei, *Appl. Phy. A.*, Volume 59, (1994) 2.
41. http://www.lpa.ens.fr/spip.php?article266&lang=en.

42. O.A. Farghaly, R. S. Abdel Hameed ,Abd-Alhakeem H. Abu-Nawwas, Int. J. Electrochem. Sci., 9(2014)3287-3318.
43. A Review of Techniques for Electrochemical Analysis, Princeton Applied Research.
44. Kissinger, P. T., Heineman, W. R., "Cyclic Voltammetry," Journal of Chemical Education, 60, 702 (1983).
45. W. Chen, D. Ghosh, S. Chen, J Mater Sci (2008) 43:5291–5299.
46. S P Mondal, S K Ray, J Ravichandran and I Manna Bull. Mater. Sci., Vol. 33, No. 4, August 2010, pp. 357–364.
47. Feng Gu, Shu Fen Wang, Chun Feng Song, Meng Kai Lu, Yong Xin Qi, Guang Jun Zhou, Dong Xu, Duo Rong Yuan. Chemical Physics Letters 372 (2003) 451-454.
48. A. N. Naje , A. S.Norry, A. M. Suhail International Journal of Innovative Research in Science,Engineering and Technology *(An ISO 3297: 2007 Certified Organization)*Vol. 2, Issue 12, December 2013.
49. J. Singh, A. Roychoudhury, M. Srivastava, P. R. Solanki, D. W. Lee, S. H. Lee and B. D. Malhotra , Nanoscale, 2014, 6, 1195.
50. J. Singh, A. Roychoudhury, M. Srivastava, P. R. Solanki, D. W. Lee, S. H. and B. D. Malhotra, J. Phys. Chem. B 2013, 117, 141−152.
51. S. M. Amininezhad, A. Rezvani, M. Amouheidari, S. M. Amininejad, S. Rakhshani, Zahedan Journal of Research in Medical Sciences Journal homepage: www.zjrms.ir.